Thermodynamic Simulation and Solidification Behavior of Multicomponent High Entropy Alloys

M.Tech. Thesis

By

AVI JAIN

DISCIPLINE OF METALLURGY ENGINEERING AND MATERIALS SCIENCE

INDIAN INSTITUTE OF TECHNOLOGY INDORE

JUNE 2019

Thermodynamic Simulation and Solidification Behavior of Multicomponent High Entropy Alloys

A THESIS

Submitted in partial fulfillment of the
requirements for the award of the degree
of
Master of Technology

by

AVI JAIN

DISCIPLINE OF METALLURGY ENGINEERING AND MATERIALS SCIENCE
INDIAN INSTITUTE OF TECHNOLOGY INDORE
JUNE 2019

INDIAN INSTITUTE OF TECHNOLOGY INDORE

CANDIDATE'S DECLARATION

I hereby certify that the work which is being presented in the thesis entitled **Thermodynamic Simulation and Solidification Behavior of Multicomponent High Entropy Alloys** in the partial fulfillment of the requirements for the award of the degree of **MASTER OF TECHNOLOGY** and submitted in the **DISCIPLINE OF METALLURGY ENGINEERING AND MATERIALS SCIENCE, Indian Institute of Technology Indore**, is an authentic record of my own work carried out during the time period from July 2017 to June 2019 under the supervision of Dr. Sumanta Samal, Assistant Professor and Dr. Mrigendra Dubey, Assistant Professor, Discipline of Metallurgy Engineering and Material Science (MEMS) Indian Institute of Technology (IIT) Indore. The matter presented in this thesis has not been submitted by me for the award of any other degree of this or any other institute.

Signature of the student with date
(AVI JAIN)

This is to certify that the above statement made by the candidate is correct to the best of my/our knowledge.

Signature of the Supervisor of
M.Tech. thesis
DR. SUMANTA SAMAL

Signature of the Supervisor of
M.Tech. thesis
DR. MRIGENDRA DUBEY

AVI JAIN has successfully given his/her M.Tech. Oral Examination held on **June 26th, 2019**

Signature(s) of Supervisor(s) of M.Tech. thesis
Date:

Convener, DPGC
Date:

Signature of PSPC Member
Date:

Signature of PSPC Member
Date:

Signature of PSPC Member
Date:

ACKNOWLEDGEMENTS

It is a pleasure to thank many people who made this work possible.

First and foremost, I would like to thank my advisors, Dr. Sumanta Samal and Dr. Mrigendra Dubey whose support and guidance have driven me to do this work. There friendly nature gave me the freedom and opportunity to interact with them as much as I wanted to.

I would like to take this opportunity to thank my PSPC members Dr P.M. Shirage, Dr. S.S. Hosmani and Dr. I.A. Palani for their valuable time in assessing my work during the mid-term and end-term presentations and giving me valuable suggestions related to my work.

I am also thankful to the HOD MEMS and the faculty of this institution for their support and effort in teaching the concepts in Materials Science and Engineering.

I thank my classmates and friends at the Institute for the good time I had here.

Finally, I thank my parents for their constant support.

DEDICATION

Dedicated To my Guide

My Parents

My Teachers

My Friends

Synopsis

Zirconium containing high entropy alloys (HEAs) such as $FeCoNiCrZr_x$, $FeCoNiCrAlZr_x$ and $FeCoNiCrCuZr_x$ (x = 0, 2.5, 5.0, 7.5, 10) are designed with the help of CALPHAD technique by using Thermocal simulation. Phase diagram obtained from the CALPHAD technique shows formation of eutectic reaction due to addition of the zirconium. The solidification pathways of the designed HEAs are understood based upon thermodynamic simulation results. Thermodynamic and Hume-Rothery parameters that govern the morphology and composition of high entropy alloys are also calculated to identify the formation of solid solution phase(s). The high entropy alloys such as $FeCoNiCrZr_x$, $FeCoNiCrAlZr_x$ and $FeCoNiCrCuZr_x$ (x = 0, 2.5, 5.0, 7.5, 10) are synthesized by vacuum arc melting cum suction casting technique.

The detailed structural and microstructural characterization are done to identify the phases and also to understand the sequence of phase evolution during solidification. $FeCoNiCrZr_{10}$ alloy exhibits bimodal eutectic morphology while $FeCoNiCrCuZr_{10}$ alloy shows hypereutectic structure with acicular structure.$FeCoNiCrZr_{10}$ HEA exhibits bimodal eutectic microstructure consisting of both lamellar eutectics (i.e. L ⟶ FCC ($\boldsymbol{\alpha}$) + Co_2Zr-type Laves phases (γ_1)) and globular eutectics (i.e. L ⟶+ FCC ($\boldsymbol{\alpha}$) + Ni_7Zr_2). The new pseudo-quasiperitectic reaction i.e. L + Laves phases (γ_1) ⟶ FCC ($\boldsymbol{\alpha}$) + + Ni_7Zr_2 has been proposed for $FeCoNiCrZr_{10}$ HEA. While $FeCoNiCrAlZr_{10}$HEA shows eutectic microstructure consisting of BCC solid solution phase and Laves phase (i.e. L → BCC solid solution (B2) + Laves phase). $FeCoNiCrCuZr_{10}$ HEA shows bimodal eutectic microstructure (i.e. L → FCC solid solution (α_1) + Laves phase and L→ FCC solid solution (α_2) + Ni_5Zr). It is found that Zr containing HEA (i.e.

$FeCoNiCrZr_{10}$HEA) shows better hardness (≃259.9 HV) as compared to other studied HEAs.

Secondly, various experiments are done using polyol process to synthesize nanoparticles of high entropy alloys. Binary alloy system of CuNi is successfully prepared through this process. In case of FeNiCu and CoNiCu, ternary alloy systems, solid solution phase is formed as a final product along with some other organometallic compounds. While in case of CoNiCr alloy system, only Cr gets reduced leaving other two.

TABLE OF CONTENTS

LIST OF FIGURES **iix**

LIST OF TABLES **ix**

ACRONYMS **x**

Chapter 1: Introduction **1**

1.1Overview **1**

1.2 High Entropy Alloys **1**

1.3 Core Effects of High Entropy Alloys **2**

1.6 Hot Deformation Behavior **5**

Chapter 2: Literature Review **6**

Chapter 3: Processing Routes **15**

3.1 Solidification Route **15**

3.2 Chemical Route **18**

Chapter 4: Methodology **21**

4.1 Microscopic Techniques **21**

4.1.1 Optical Microscopy **21**

4.1.2 Scanning Electron Microscopy(SEM) **21**

4.1.3 Energy Dispersive Spectroscopy(EDS) **22**

4.2 Mechanical Experiments **22**

4.2.1Vickers Hardness Test **22**

4.2.2 Hot Deformation Behavior **22**

4.3 Phase Analysis **23**

4.3.1 X-ray Diffractometer (XRD) **23**

4.3.2 Fourier Transform Infrared **23**

Spectroscopy

Chapter 5 Thermodynamic Simulation **36**

Chapter 6 Results and Discussion **36**
6.1 Parameter Calculation for Design of HEAs **36**
6.2 Characterization of HEAs synthesized through Solidification route **41**
6.2.1 Structural Characterization **41**
6.2.2 Microstructural Characterization **43**
6.3 Characterization of multicomponent alloys synthesized through chemical route **53**
6.3.1 Structural Characterization of Binary Alloys **53**
6.3.2 Spectroscopic analysis of Binary alloys **54**
6.3.3 Structural and spectroscopic characterization of Ternary alloys **55**
6.3.4 Structural and spectroscopic characterization of quaternary alloy **61**
Chapter7 Mechanical Properties HEAs **63**
7.1 Hardness measurement for HEAs **63**
7.2 Hot Deformation Behavior **65**
Chapter8 Conclusion and Future Scope **67**
8.1 Conclusion **67**
8.2 Scope for future work **68**
References **69**

LIST OF FIGURES

Fig. 3.1 processing route of Polyol technique 20

Fig. 5.1 a) Phase diagram b) Phase fraction Vs Temperature Phase diagram c) Solidification diagram of FeCoNiCr HEA 27

Fig. 5.2 a) Phase diagram b) Phase fraction Vs Temperature Phase diagram c) Solidification diagram of $FeCoNiCrZr_{10}$ HEA 29

Fig. 5.3a) Phase diagram b) Phase fraction Vs Temperature Phase diagram c) Solidification diagram of FeCoNiCrAl HEA 31

Fig. 5.4 a) Phase diagram b) Phase fraction Vs Temperature Phase diagram c) Solidification diagram of $FeCoNiCrAlZr_{10}$ HEA 33

Fig. 5.5 a) Phase diagram b) Phase fraction Vs Temperature Phase diagram c) Solidification diagram of $FeCoNiCrCuZr_{10}$ HEA 35

Fig 6.1 XRD pattern of $FeCoNiCrZr_x$ (X= 0, 2.5, 5.0, 7.5, 10) samples 41

Fig. 6.2 XRD pattern of $FeCoNiCrAlZr_x$ (X= 0, 2.5, 5.0, 7.5, 10) samples 42

Fig. 6.3 XRD pattern of $FeCoNiCrCuZr_x$ (X= 0, 2.5, 5.0, 7.5, 10) samples 43

Fig. 6.4 Optical micrograph of $FeCoNiCrZr_x$ (X = 0, 2.5, 5.0, 7.5, 10) samples 44

Fig.6.5 Optical micrograph of $FeCoNiCrAlZr_x$ (X=0, 2.5, 5.0, 7.5, 10) samples 45

Fig. 6.6 Optical micrograph of $FeCoNiCrCuZr_x$ (X = 2.5, 5.0, 7.5, 10) samples 46

Fig. 6.7 Low magnification SEM images of $FeCoNiCrZr_x$ (0, 7.5, 10) samples 47

Fig. 6.8 High magnification SEM images of $FeCoNiCrZr_x$ (X = 0, 7.5, 10) samples 47

Fig. 6.9 a) EDS mapping for darker region in $FeCoNiCrZr_{7.5}$ HEA b) EDS mapping for brighter region $FeCoNiCrZr_{7.5}$ HEA 48

Fig. 6.10 EDS mapping of brighter region of $FeCoNiCrZr_{10}$ HEA 49
Fig. 6.11 SEM images in BSE mode for $FeCoNiCrCuZr_x$ (x = 2.5, 5.0, 7.5, 10) samples 50
Fig. 6.12 EDS mapping of $FeCoNiCrCuZr_{2.5}$ HEA 51
Fig. 6.13 EDS mapping of $FeCoNiCrCuZr_{5.0}$ HEA 51
Fig. 6.14 EDS mapping of $FeCoNiCrCuZr_{7.5}$ HEA 52
Fig. 6.15 EDS mapping of $FeCoNiCrCuZr_{10}$ HEA 53
Fig. 6.16 a) X-ray diffraction pattern b) FTIR pattern for CuNi alloy 55
Fig. 6.17 a) X– ray diffraction for FeNiCu b) FTIR spectrum of FeNiCu alloy c) SEM image d) EDS mapping for FeNiCu alloy 56
Fig. 6.18 a) X– ray diffraction for CoNiCr b) FTIR spectrum of CoNiCr alloy c) SEM image d) EDS mapping for CoNiCr alloy 58
Fig. 6.19 a) XRD pattern of CoNiCu b) FTIR spectrum of CoNiCu alloy c) SEM image d) EDS mapping for CoNiCu alloy 60
Fig. 6.20 a) XRD pattern of FeCoNiCu b) FTIR spectra of FeCoNiCu alloy 62
Bar chart 7.1 shows Hardness value for $FeCoNiCrZr_x$ (X = 0, 2.5, 5.0, 7.5, 10) HEAs 63
Bar chart 7.2 shows Hardness value for $FeCoNiCrAlZr_x$ (X = 0, 2.5, 5.0, 7.5, 10) HEAs 64
Bar chart 7.3 shows Hardness value for $FeCoNiCrCuZr_x$ (X = 0, 2.5, 5.0, 7.5, 10) HEAs 64
Fig. 7.1 Gleeble test of FeCoNicrAl HEA at $0.1s^{-1}$ strain rate 65

LIST OF TABLES

Table 6.1 a) Thermodynamic and b) Hume Rothery Parameters $FeCoNiCrZr_x$ 37

Table 6.2 a) Thermodynamic and b) Hume Rothery Parameters $FeCoNiCrAlZr_x$ 38

Table 6.3 a) Thermodynamic and b) Hume Rothery Parameters $FeCoNiCrCuZr_x$ 40

Table 6.4 EDX mapping of $FeCoNiCrZr_{7.5}$ 49

Table 6.5 EDX mapping of $FeCoNiCrZr_{10}$ 49

Table 6.6 EDX mapping of $FeCoNiCrCuZr_{2.5}$ 51

Table 6.7 EDX mapping of $FeCoNiCrCuZr_{5.0}$ 52

Table 6.8 EDX mapping of $FeCoNiCrZr_{7.5}$ 52

Table 6.9 EDX mapping of $FeCoNiCrCuZr_{10}$ 53

ACRONYMS

BCC	Body centered cubic
EBSD	Electron backscatter diffraction
EDX	Energy dispersive X-ray spectroscopy
FCC	Face centered cubic
HEA	High-entropy alloys
SEM	Scanning electron microscope
XRD	X-ray powder diffraction
FTIR	Fourier Transform Infrared Spectroscopy

Chapter 1

Introduction

1.1 Overview

In this thesis, the mechanical behavior of the HEAs synthesized by the solidification route has been studied for potential structural applications. Secondly, nanoparticles of multicomponent alloys have been developed using chemical route for potential functional applications.

1.2 High Entropy Alloys

Recently, high-entropy alloys (HEAs) have attracted increasing attention because of their unique compositions, microstructures, and adjustable properties. High entropy alloys are defined as the solid solution alloys composed of at least five principal elements in equal or nearly equal atomic percent (at. %)[1]. Normally principal elements are defined as the elements having composition more than five percent of atomic fraction. This alloys are coined as HEAs by Yeh et al. and named as multicomponent alloys by Cantor et al [2].

Cantor et al. pointed out that a conventional alloy development strategy leads to an enormous amount of knowledge about alloys based on one or two components, but little or no knowledge about alloys containing several main components in near-equal proportions[3]. Theoretical and experimental works on the occurrence, structure, and properties of crystalline phases have been restricted to alloys based on one or two main components. Thus, the information and understanding are highly developed on alloys close to the corners and edges of a multicomponent phase diagram, with much less knowledge about alloys located at the center of the phase diagram. This imbalance is significant for ternary alloys, but becomes rapidly much more pronounced as the number of components increases. For most quaternary and other higher-order systems, information about alloys at the center of the phase diagram is

virtually nonexistent except those HEA systems that have been reported recently.

High entropy of mixing stabilizes disordered solid solutions. However, the entropy term decreases linearly with a decrease in temperature. Ordered intermetallic phases have considerably smaller enthalpy of formation than the random solid solutions. With a decrease in temperature, diffusion and thus kinetics of phase transformations slow down. For use in elevated temperature applications, the microstructure of HEAs must be stable, because any phase transformations occurring during use could deteriorate properties, initiate creep or failure. At the same time, suppressed kinetics may lead to precipitation of very fine, nanometer-sized particles and considerably improve properties of these alloys at ambient temperatures. Therefore, as candidate materials for high-temperature structural applications, studying of phase and microstructure stability in HEAs is particularly beneficial.

1.3 Core effects of High Entropy Alloys

The HEAs consist of five or more components forming a complex system whose properties and structure mainly depends on four core effects. Yeh suggested four core effects that describe the properties of HEAs[3]:

(1) High entropy effects

High-entropy effect is the most important effect because it can enhance the formation of solid solutions and makes the microstructure much simpler than expected. High entropy effect helps in the formation of simpler solid solution in HEAs rather than formation of different intermetallics specially at higher temperatures [3]. The high entropy effect facilitates the formation of disordered solid solution rather than ordered intermetallics compound. Elemental phases have small negative ΔH_{mix} and ΔS_{mix} because they are based on one major element. Compound phases have large negative ΔH_{mix} but small ΔS_{mix} because ordered structures have

small configurational entropy. But random solid solution phases containing multicomponents have medium negative ΔH_{mix} and highest ΔS_{mix}.

As the Gibbs free energy of mixing, ΔG_{mix}, is

$$\Delta G_{mix} = \Delta H_{mix} - T\Delta S_{mix}$$

where ΔH_{mix} and ΔS_{mix} are the enthalpy of mixing and entropy of mixing, respectively, higher number of element would potentially lower the mixing free energy, especially at high temperatures by contributing larger ΔS_{mix}. Therefore, disordered solid solution phase is more stable at high temperature than ordered intermetallic phases. It enhances the formation of solid solution phase due to which solution hardening take place in solution phase causing increase in the strength and ductility of HEAs. The stronger bond energies will enhance the formation of solid solution rather than intermetallics.

(2) Sluggish diffusion effect

HEAs consist of random solid solution phases along with ordered solid solution, causing sluggish diffusion of atoms and vacancies leading to chemical stability of the HEAs. A vacancy in the whole-solute matrix is in fact surrounded and competed by different-element atoms during diffusion. It has been proposed that slower diffusion and higher activation energy would occur in HEAs due to larger fluctuation of lattice potential energy (LPE) between lattice sites. The abundant low-LPE sites can serve as traps and hinder the diffusion of atoms. This leads to the sluggish diffusion effect.

It is expected that sluggish diffusion might affect phase nucleation, growth and distribution, and morphology of new phase through diffusion controlled phase transformation.

Sluggish diffusion helps in improving the properties and microstructure of the HEAs. As sluggish diffusion leads to finer grain structure causing good toughness and strength. It also improves the creep property causing prolong life at high temperature.

(3) Severe lattice distortion effect

It is important to note that due to multicomponent matrix of different solid solution phases in HEAs, each atom is surrounded by different kind of atom thus causing severe lattice strain and stress due to the atomic size difference.

Along with different atomic size difference, different bonding energy and crystal structure of consisting elements also leads to higher lattice strain. Lattice distortion not only affects various properties but also reduces the thermal effect on properties. Lattice distortion causes significant electronic scattering leading to decrease in electrical conductivity of HEAs. Phonon scattering is also large in HEAs due to severe lattice distortion leading to decrease in the thermal conductivity.

Lattice distortion caused by thermal vibration is less than the severe lattice distortion in HEAs causing it insensitive towards the change of temperature.

(4) *Cocktail effects*

This term is coined by Prof. Ranganathan to study the properties that gets enhanced in HEAs[4]. The enhancement of properties of HEAs may be due to interaction of different properties of different constituent phases present in HEAs. Generally, mixture rule is used to calculate the value of properties in conventional alloy system but when same rule is applied in HEAs. There is severe difference in the experimental value and value that obtained from the mixture rule. This variation in property of HEAs arises not only due to basic properties of elements by the mixture rule but also

from the mutual interactions among all the elements and from the severe lattice distortion. Mutual interaction and Lattice distortion also lead to great change in the quantified values of the properties in case of HEAs. The cocktail effect brings many positive effects in HEAs such as high magnetization, low coercivity, good plasticity, high strength, and high electrical resistance.

1.4Hot Deformation Behavior

Hot deformation is an essential step in the processing route of industrial alloys. The energy required for a shape change through hot working (Q_d) directly depends on the alloy deformation resistance. Measuring this energy is crucial to the industrial design as well as to the scientific community. Hence, many papers have been devoted so far to calculate Q_d for the hot deformation of different alloys. Due to the fact that Q_d depends on the deformation resistance, its value is calculated by using different constitutive descriptions of flow stress[5]. The value of Q_d strongly depends on the material characteristics, which is particularly controlled by the mechanism of dynamic softening, dynamic recovery (DRV), or dynamic recrystallization (DRX). As a matter of fact, there is a relationship between the stacking fault energy (SFE) and the deformation resistance or Qd. In practice, the value of Q_d is often lower for high-SFE metals which are prone to DRV such as Al and ferritic stainless steels than low SFE ones such as austenite, which undergo DRX[5]. However, there have been controversies over the exact mechanism. Although the mechanism of dynamic softening affects the required activation energy, it is apparent that Q_d should depend on the applied temperature and deformation. It has been understood that the deformation resistance or Q_d depends on how easily the dislocations can overcome the obstacles during plastic deformation.

.

Chapter 2

Literature Review

HEAs were first reported in 1996 by J.W. Yeh and K.H. Huang. Multi component high entropy alloy is currently emerging as a new field to researchers of metallic materials community[6][7][8]. HEAs generally consist of five or more principle elements instead of one or two as in case of conventional alloys. Discover of HEAs is a breakthrough in the field of metallurgy as it lead to exploration of new materials and new properties. HEA exhibits excellent physicochemical properties such as special electrical and magnetic properties[9], a high strength as well as promising resistances to wear, oxidation and corrosion[10][11][12], making them promising candidates for future engineering applications.

From the literature, it is found that HEAs have a high softening resistance at elevated temperatures[1][13] and sluggish diffusion kinetics[14]. Therefore, it is seen as a future material for high temperature application. Before using it for high temperature application, there is some technical challenge related to mechanical properties which need to be solved. In case of HEAs having single phase there is problem related to balancing of ductility and tensile strength[6][7]. As in case of HEAs having single phase fcc structure, we get good ductility but not enough strength [15][16]while in case of single phase bcc structure HEA, we have good strength along with brittleness[17]. Therefore to solve this problem researchers are now working in the direction of composite HEAs. However simply adding both fcc and bcc phases without proper structural design cannot solve this problem[18]. It may also lead to the deterioration in the mechanical properties of the HEAs.

There are other difficulties also which downgrade the mechanical properties of HEAs and hinder the use of HEAs for engineering application. Poor castability along with compositional segregation of constituent phases are the major problems that downgrade the properties and limit the use of HEAs for engineering application[8][19].

So as to solve the above challenges related to HEAs researches come up with the idea of eutectic alloys which is used to develop a composite HEAs. The idea is to develop a eutectic alloy having mixture of both fcc and bcc phases providing good ductility along with good strength. This HEA should contain soft fcc phases along with hard bcc phases, which helps in providing reasonable balance between high fractural strength and high ductility. There are other advantages also in the use of eutectic alloys [20]. They are as follows [21]:

i) Eutectic alloys have microstructures which are very near to equilibrium causing greater resistance to high temperature along with having greater reaction temperature.

ii) Low energy phase boundaries

iii) Controllable microstructures

iv) High rupture strength

v) Stable defect structures

vi) Excellent high-temperature creep resistance

vii) Regular lamellar or rod-like eutectic organization, forming an in-situ composite

Along with above advantages that are used to solve first problem related to mechanical properties of HEAs. The problem of poor castability can also be resolved by use of eutectic alloys. Also important to know that in eutectic reaction the solidification transformation takes place at isothermal

temperature so there is no solidification temperature range causing problem of phase segregation along with shrinkage cavity to be solved[20].

There are various techniques for manufacturing of HEAs such as arc melting, mechanical alloying, laser cladding, thin film sputtering etc. The most widely technique for the synthesis of HEAs is the melting and casting route. Melting and casting route is used widely because it can reach melting temperature of about 3273K which can melt most of the metals used for making HEAs. It is also economical and feasible process thus attracting significant attention from both the academia and the industry field.

Due to size reduction of particle its property improves leading to increase in the application potential of HEAs. Metallic nanoparticles due to their unique properties are attracting lot of attraction from the academia and industry. Due to reduction in their size metallic nanoparticles shows unique physicochemical properties to their bulk counterparts. Many physicochemical properties such as magnetic, catalytic and biomedical properties gets improved for HEAs as their size decreases[22]. Therefore, nanoparticle of HEA has become attractive topic for researches.

Many researches are working in this field by synthesizing them through mechanical alloying method. But this technique has some limitation causing to poor results. One of the great limitations of this method is that grains produce is usually of larger size (> 30nm). This also leads to the agglomeration of nano-grains into larger grains of size larger than 3μm[23][24]. In mechanical alloying technique, the nanoparticles produce does not have homogeneous chemical composition and have no control over the growth process.

Polyol process is a rapid and economical synthesis technique for the fabrication of particulate products and has been widely used for the

synthesis of a variety of metal and alloy nanoparticles, forming nano-sized, homogeneous, and highly reactive powders through mixing different metallic salts in the polyols [25]. Many bimetallic alloys such as Fe-Pt, Cu-Ni are been developed by polyol process showing a great potential of this method for the synthesis of nanocrystalline HEAs[26].

HEAs forms disordered and partially ordered solid solution phases having FCC, BCC, or HCP structures, instead of a mixture of many intermetallics due to the high configurational entropy possessed by these alloys. As we know FeCoNiCr forms a single phase face centered structure which has good ductility but poor yield strength while in case of FeCoNiCrAl HEA, we have bcc structure with good yield strength but low ductility[27].

Outcomes of Literature Review

1. To develop composite of eutectic HEAs having balance of mechanical properties.
2. Limited study on hot deformation behavior of HEAs.
3. Simulated study of HEAs has not been highlighted extensively.
4. Limited study on development of the nanoparticles HEAs through chemical route.

Objective of our project

1. To synthesize Novel HEAs by Solidification route and Chemical synthesis method.
2. To understand the stability of HEAs i.e. both chemical and thermal stability.
3. To study the deformation behavior of designed HEAs at different temperature and strain rate.

Stable Solid Solution Formation Criteria for High Entropy Alloys

To predict the phase stability of the HEAs from fundamental properties of the constituent elements is used by many as the starting point in the development of the HEAs. Here we focus on the properties of the individual elements and their interaction with the other alloying elements. The idea here is to find out the rules governing the phase stability in HEAs by statistically analyzing the collective behavior of the constituent elements in a large database of HEAs, where different phases form, including amorphous phases, solid solution phases or intermetallic phases. .Some parameters are thermodynamic parameters while other is size parameters. First attempt to study the stability of HEAs was done by Zhang et al [1]. They use three parameters to predict the stability and phase involved in the HEA system.

Various parameters taken into account in our project are as follows:

i. Gibbs free energy (ΔG_{mix})

The Gibbs free energy change of mixing determines whether the process is spontaneous at a given pressure and temperature. This quantity combines two physical effects—the enthalpy of mixing, which is a measure of the energy change, and the entropy of mixing considered here.

$$\Delta_{mix} G = \Delta_{mix} H - T \Delta_{mix} S \qquad \ldots[28]$$

Where, $\Delta_{mix} H$ = Change of Enthalpy

T = Temperature

$\Delta_{mix} S$ = Change of Entropy

In HEAs, Gibbs free energy must be lowed to form an stable phases.

ii. Enthalpy of Mixing ($\Delta_{mix} H$)

Enthalpy is defined as thermodynamic quantity equivalent to the total heat content of a system. It is equal to the internal energy of the system plus the product of pressure and volume. Enthalpy of Mixing for HEAs is given by[28];

$$\Delta H_{mix} = \sum_{i=1, i\neq j}^{n} \Omega_{ij} c_i c_j ; \left(\Omega_{ij} = 4\Delta H_{AB}^{mix}\right)$$

Where, ΔH_{AB}^{mix} = Enthalpy of Mixing of binary liquid alloy AB,

C_i = Concentration of i^{th} element

iii. Configuration Entropy ($\Delta_{mix}S$)

Configuration entropy is described as the portion of the entropy related to the discrete representative position of its constituent particles. The configuration entropy of a crystal refers to the distinguishable ways the atoms can be arranged on the lattice sites.

$$\Delta S_{mix} = -R\sum_{i=1}^{n} (c_i \ln c_i) \quad \text{... [28]}$$

For HEAs alloy the value of configuration entropy is between 12 to 17.5 J/ K mol.

iv. Thermodynamic Parameters

As we know both enthalpy of mixing and configuration entropy plays opposite role in the formation of solid solution. So by comparing the values of $\Delta_{mix}H$ and $T\Delta_{mix}S$, we can judge the formation solid solution. Although the enthalpy of mixing is absolute larger, which is often in kJ mol^{-1}, $T\Delta S_{mix}$ could be compared with the enthalpy of mixing at high temperature. At high temperature the effect of the HE of mixing could overcome the effect of the enthalpy of mixing, $T\Delta S_{mix}$ become the main

factor affecting the solid-solution formation. So to deal with both factors a new factor called Thermodynamic Parameter is defined[28]. It is represented by Ω.

$$\Omega = \frac{T_m \Delta S_{mix}}{\left|\Delta H_{mix}\right|}$$

For solid solution formation, the value of Ω must be positive and $\Omega = 1$ should be proposed as a critical value to form the solid solution. If $\Omega > 1$, the contribution of $T\Delta S_{mix}$ will exceed that of ΔH_{mix} for solid-solution formation, and the multi-component HEAs are mainly composed of the solid solutions; if $\Omega \leq 1$, ΔH_{mix} is the predominant part of the free energy, and intermetallic compounds and segregations are prior to solid-solution phases to form in HEAs. Thus the value of Ω is used to estimate the solid-solution formation ability.

In this melting point (T_m) is calculated by Vagard's mixture rule,

$$T_m = \sum_{i=1}^{n} c_i \left(T_m\right)_i \qquad \text{....[28]}$$

v. Atomic size difference (δ)

The atomic size difference factor is used to describe the effect of size of constituent elements on the formation of solid solution.

$$\delta = \sqrt{\sum_{i=1}^{n} c_i \left(1 - \frac{r_1}{\bar{r}}\right)^2}$$

Where, r_i is the radius of the i^{th} element and $\bar{r}$ is the mean radius of all the elements given by,

$$\bar{r} = \sum_{i=1}^{n} c_i r_i$$

vi. Valence electron concentration (VEC)

Valence electron concentration determines the structure of the solid solution formed in HEAs.

Here VEC is calculated using mixture rule,

$$VEC = \sum_{i=1}^{n} c_i (VEC)_i$$

Where $(VEC)_i$ is the valence electron concentration of the i^{th} element.

(i) ≥ 8.0 (FCC phase only)

(ii) 6.87 ≤ VEC < 8.0 (FCC and BCC phase co-exist)

(iii) < 6.87 (BCC phase only)

vi. Electronegativity (Δ□)

The electronegativity difference among constituents determines the formation of intermetallics in any complex alloy system. In HEAs also electronegativity difference between different constituting elements plays a important role in the formation of intermetallics [29];

$$\Delta\chi = \sqrt{\sum_{i=1}^{n} c_i \left(\chi_i - \bar{\chi}\right)^2}$$

Where

□$_i$ is the pauling electronegativity for the i^{th} element.

$$\overline{\chi} = \sum_{i=1}^{n} c_i \chi_i$$

vii. Λ – Parameter

As we know that configuration entropy ΔS_{mix} increases the possibility of solid solution formation while on the other hand atomic size difference ∂ acts in the opposite way by decreasing the probability of formation of solid solution. So to study the effect of both factor simultaneously geometric factor is used[30];

$$\Lambda = \Delta S_{mix} / \delta^2$$

The Λ – Parameter is used to guide the nature of the compound formed and its volume fraction.

For the formation of single phase DSS $\Lambda > 0.96$

Solid solution Phase mixtures $0.24 < \Lambda < 0.96$ and

Mixtures containing solid solution phases with intermetallics when $\Lambda <$ 0.24.

Chapter 3

Processing Routes

The HEAs materials can be processed through different manufacturing routes, and to fully explore the possibilities for high throughput fabrication, all possible techniques should be considered. This section will cover two particular techniques used for the synthesis of HEAs materials in this project.

3.1 **Solidification Route**

Solidification route is the most widely used method for the synthesis of the HEAs. Vacuum arc melting is used vastly for the formation of the both equimolar and non–equimolar HEAs. The vacuum arc melting process is most popular because here temperature obtained is very high (upto 3000° C) which can be used to melt most of the metals needed in the preparation of HEAs. The disadvantage of this method is that there is the possibility of evaporation of certain low boiling metals like aluminum, copper during preparation of HEAs making composition control difficult.

Vacuum arc melting is a process for the production of metal ingots with high chemical and mechanical homogeneity. In over project we are using vacuum arc melting cum casting unit to synthesis samples.

It consists of three units:-

i. Vacuum unit

ii. Welding unit

iii. Chilling unit

Vacuum unit

In vacuum unit vacuum and turbo pump are used to generate the vacuum in the chamber. The switches used in it are pneumatic control powered by the compressor of 2HP. The vacuum chamber consists of the water cooled copper die in which metals gets melted with the help of tungsten electrode. Direct current is used to generate the arc in the presence of the argon atmosphere. The electrode is maintained at constant arc length during melting and the electric arc is maintained by a DC power supply connected to the electrode and the die. The electrode can reach upto 3000°C temperature.

Image of Vacuum Unit

Welding unit

This is a simple TIG welding unit used as a constant DC power supply source. Max voltage is 30V while max current reached is 400A. It is used as a DC power supply to supply current at constant rate so as to maintain proper arc.

Image of Welding unit

Chilling unit

The vacuum arc melting cum casting unit is also provided with a chilling unit which supplies cold water to copper die and electrode. It is used to maintain temperature of the die and electrode. It helps in fast cooling of the die and electrode.

Image of Cooling Unit

Advantages:

i. The high temperature and high vacuum environment helps in the removal of entrapped gases and high pressure elements.
ii. The high melting temperature produces the segregation of metallic and non metallic inclusion.
iii. High density with desirable grain structure and low macro. The typical grain structure of parts produced by arc melting consists of columnar for small diameter parts or a mixture of columnar and equi-axed grains for larger parts.

Disadvantages

This technique cannot be used for low melting point materials such as Mg, Zn, Mn where it cannot control the composition of the alloys.

Procedure

The multi-components $FeCoNiCrZr_x$,$FeCoNiCrAlZr_x$ and $FeCoNiCrCuZr_x$ were prepared by arc melting cum casting machine from highly pure Co, Fe, Cr ,Ni and Zr elements in a Ti-gettered ultra high-purity argon atmosphere to get arc melted alloy button. The alloy button was re-melted 5–6 times to make sure that the alloy was chemically homogenized in liquid state. Further, buttons were suction casted in the form of cylindrical rod having 6 mm diameter.

3.2 Chemical Route

Polyol method is a robust strategy for preparation of well-defined metal nanoparticles in terms of size, shape, composition and crystallinity. In polyol process there is reduction of metal precursors in the presence of some capping agent at elevated temperature. The polyol process is first

used by Fievets group in 1989 for the synthesis of metal nanoparticles. It is a versatile liquid-phase method utilizing high boiling and multivalent alcohols to produce nanoparticles. Polyols is an organic compound having multiple hydroxyl groups. It this polyol plays dual role of solvent and reducing agent for metal precursors. It also helps in controlling the growth of the metallic nanoparticles.

Advantages of Polyol synthesis route:

i. High boiling point of polyols helps in reaching high reaction temperature of 473-593K without the use of high pressure and autoclave.
ii. Good solubility of metallic precursors in polyols helps as to use cheap and simple precursors as starting reactants.
iii. Chelating ability of polyols is a key factor that helps in controlling the nucleation, growth and agglomeration of nanoparticles.
iv. Reductive ability of polyols at high temperature helps in reducing the metal solution into nanoparticles.

Procedure

All hydrated metal salts (acetates, hydroxides, and chlorides), polyols ethylene glycol (EG), propylene glycol (PG), diethylene glycol (DEG), tetraethylene glycol (TEG), and butylene glycol (BG), NaOH, and methanol were used without any further purification. The general procedure involves the preparation of 0.1 M metal salt in 25 mL of polyol, followed by the addition of NaOH (1.0 M). A small amount of $AgNO_3$ is added as a nucleating agent. Then the mixture is heated in programmable electric oven for about 3hrs at 180℃ (Figure 3.1). Final products were centrifuged and washed several times with methanol. The samples were then dried in a vacuum oven at room temperature (25°C) prior to analysis.

Processing route of Polyol method

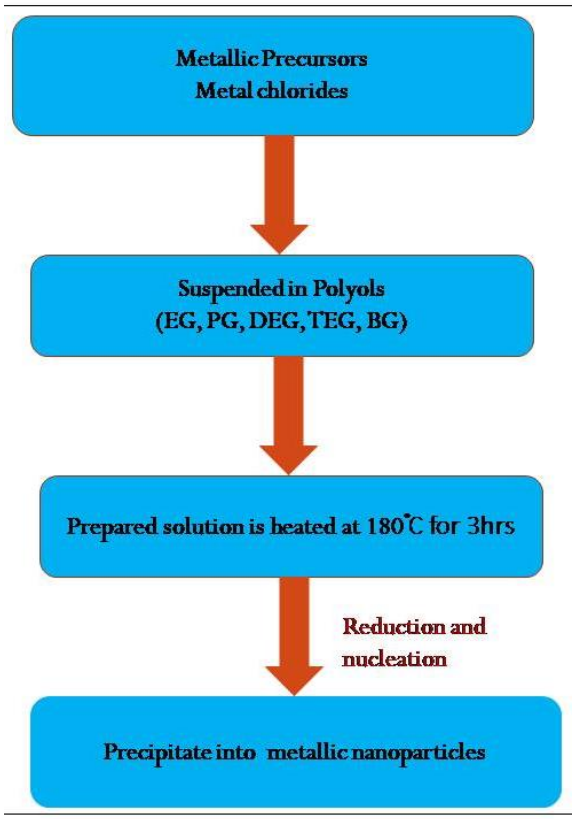

Fig. 3.1 Processing route of Polyol technique

Chapter 4

Methodology

4.1 Microscopic techniques

4.1.1 Optical Microscopy

Optical microscopy functions by the transmission of light through a material or reflection of light from a material surface. Objects are usually placed in the focal plane of a lens. In metallic materials, optical microscopes are used for preliminary evaluation of a material surface to determine surface roughness and whether the sample can be evaluated with other microscopic techniques requiring flat surfaces to determine other microstructural features. It is mostly used at mechanical polishing intervals for metal and alloys and comes in handy for quick analysis. It gives a general overview of a material, though limitations exist due to the resolution limit of submicron particles approaching the wavelength of visible light (400 to 700 nm). The Carl Zeiss Axiovert A1inverted microscope was used in our preliminary studies.

4.1.2. Scanning Electron Microscopy (SEM)

This microscopic technique works at very small wavelengths (3.7 pm at 100 KeV) and electrons are deflected by a magnetic field. Electrons interact with particles of the material, and several characteristic signals such as backscattered electrons, secondary electrons, x-rays, etc. are obtained. These signals can be used to get a further understanding of the material structure by coupling with appropriate detectors. The backscatter electrons are high energy electrons reflected from the sample surface via elastic scattering. This is useful for phase contrast analysis due to atomic size contrasts of different elements. The secondary electrons are low energy electrons obtained from few nanometers interaction 22 with the sample surface via inelastic scattering. Imaging with this technique

ensures a better surface topography. Consequently, very small surface features can be identified, such as grain boundaries, pore, voids, inclusions, precipitates, etc. SEMs can be used to study surface morphology and topography of materials at a resolution of 10 nm. It is therefore an essential tool for texture analysis. In this study, the INSPECT F SEM coupled with a Back-Scatter detector and the FEI dual beam SEM coupled with the secondary electron detectors were used.

4.1.3 Energy Dispersive Spectroscopy (EDS)

The energy dispersive spectroscopy (EDS) technique is usually coupled with the SEM to evaluate the elemental composition of a material. Characteristic X-ray signals unique to individual elements are obtained from the SEM and this can be used to probe elemental constituents in a material, either by line scans, mapping, or point analysis at specific sites. The INSPECT F SEM coupled with Oxford INCA 300 X-ray Energy Dispersive Spectrometer (EDS) was used in this study.

4.2 Mechanical experiments

4.2.1 Vickers Hardness Test

Hardness is a characteristic of a material, not a fundamental physical property. It is defined as the resistance to indentation, and it is determined by measuring the permanent depth of the indentation. A square base pyramid shaped diamond is used for testing in the Vickers scale.

4.2.2 Hot Deformation Behavior

To understand the deformation of HEAs at high temperature and at different strain rates, we used Gleeble 3800 – GTC thermo – mechanical simulator coupled with general MCU is used to perform isothermal hot compression tests. Specimen used is cylindrical rod (Ø 6 mm and aspect ratio of 1.5:1). The cylindrical specimen was deformed to approximately 50% reduction in the height.

4.3 Phase Analysis

4.3.1 X ray Diffraction (XRD)

X-ray powder diffraction (XRD) is a rapid analytical technique primarily used for phase identification of a crystalline material and can provide information on unit cell dimensions. The interaction of the incident rays with the sample produces constructive interference (and a diffracted ray) when conditions satisfy Bragg's Law ($n\lambda=2d\sin\theta$). This law relates the wavelength of electromagnetic radiation to the diffraction angle and the lattice spacing in a crystalline sample. These diffracted X-rays are then detected, processed and counted. The crystal structure of studied HEA was identified by Bruker D2 phaser X-ray diffractometer with Cu-K_α ($\lambda = 1.54056$ Å) radiation, operating at 45 kV and 30 mA, with step size of $2\theta = 0.017°$

4.3.2 Fourier Transform Infrared Spectroscopy (FTIR)

Fourier-transform infrared spectroscopy (FTIR) is a technique used to obtain an infrared spectrum of absorption or emission of a solid, liquid or gas. Infrared spectroscopy (IR spectroscopy or vibrational spectroscopy) involves the interaction of infrared radiation with matter. It covers a range of techniques, mostly based on absorption spectroscopy. As with all spectroscopic techniques, it can be used to identify and study chemicals. IR spectroscopy is often used to identify structures because functional groups give rise to characteristic bands both in terms of intensity and position (frequency). To study the functional group mid infrared band of 4000-400 cm^{-1} is used. The mid infrared region is used to study the fundamental vibrations and associated rotational vibration of the functional group associated with the sample. To identify the functional groups Perkin Elmer FTIR spectrometer is used with mid infrared band of wave number 4000- 350 cm^{-1} and wavelength of 2.5 – 25μm.

Chapter 5

Thermodynamic Simulation

Phase diagrams are the essential factor in the development of high-entropy alloy formation. Long-term stability of high entropy alloys (HEAs) at high temperature is a critical factor in the design and practical application of HEAs. It has been discovered that many HEAs have a kinetically-stabilized metastable phases, and recent experimental studies have confirmed this result by observing HEA decomposition after long-term equilibration[31]. In our project, we demonstrate the use of the CALculation of PHAse Diagrams (CALPHAD) approach for the prediction of HEA stability.

Thermodynamic and phase equilibrium data are used to determine Gibbs free energies of individual phases in the system. For a solid solution phase, α, the Gibbs free energy (G_α) is defined by,

$$G^{\alpha} = \sum_i^c X_i \, G_i^{\alpha} - TS_{mix}^{ideal} + {}^{xs}G_{\mathrm{m}}$$

Where, x_i is the composition of component i^{th}, G_i^{α} Gibbs energy of i^{th} component in the α phase, T is the temperature, S_{mix}^{ideal} is the ideal configurational entropy (i.e., $R\sum x_i \ln x_i$, where R is the universal gas constant.) and ${}^{xs}G_m$ is the excess Gibbs energy. Databases containing these free energy descriptions are used for the prediction of phase equilibrium and other properties for large, multicomponent alloys at various compositions by combining the data of simpler subsystems.

For complex solid solution systems (such as HEAs), the CALPHAD approach help us to predict the thermodynamic properties, such as phase stability accurately. In CALPHAD approach both ideal configuration entropy and excess Gibbs energy are taken into account for predicting the stability of HEAs The excess Gibbs energy (${}^{xs}G_m$) corresponding to the

non-ideal mixing enthalpy and entropy and is defined by a Redlich-Kister polynomial in CALPHAD;

$$^{xs}G_m = \sum_{i=1}^{c-1}\sum_{j>i}^{c} x_i x_j \sum_{v=0}^{n} {}^{v}L_{ij}(x_i - x_j)^v + \sum_{i=1}^{c-2}\sum_{j>i}^{c-1}\sum_{k>j}^{c} x_i x_j x_k {}^{0}L_{ijk} \quad [31]$$

Where x_i is the composition of i^{th} component, ${}^{v}L_{ij}$ are the binary interaction parameters that determines the non-ideality of the binary solid solution between components i and j, v is the order of the interaction (e.g., 0 is regular, 1 is sub-regular, etc.), and ${}^{0}L_{ijk}$ is the regular ternary solution interaction parameter for elements i, j and k. The dependence of the L parameters on the temperature defines an excess entropy contribution to the system. The interaction parameters are compared to experimental or theoretically predicted thermodynamic data. For a large number of components, the solid-solution thermodynamics parameters are predicted by summing over all of the subsystem interactions parameters. Generally ideal configuration entropy acts as a stabilizing force for the HEAs.

Thermodynamic Simulations

The thermodynamic simulation is done to predict the phases formed in alloys to determine the properties of the alloy system. To predict the phases develop in HEAs thermodynamically, CALPHAD approach is used. In CALPHAD approach various thermodynamic functions such as Gibbs energy (G), Helmholtz energy (A) etc are used to evaluate different phases that may form.

The phase diagram for FeCoNiCr system is shown in Fig. 1a. The phase diagram of FeCoNiCr suggests the liquid is completely converted into FCC(L12) phase. From figure 1b and c it is concluded that the entire liquid is converted into FCC (L12) phase. FeCoNiCr completely solidified into FCC (L12) phase. Fig. 1b also suggests the effect of heat treatment on FeCoNiCr system.

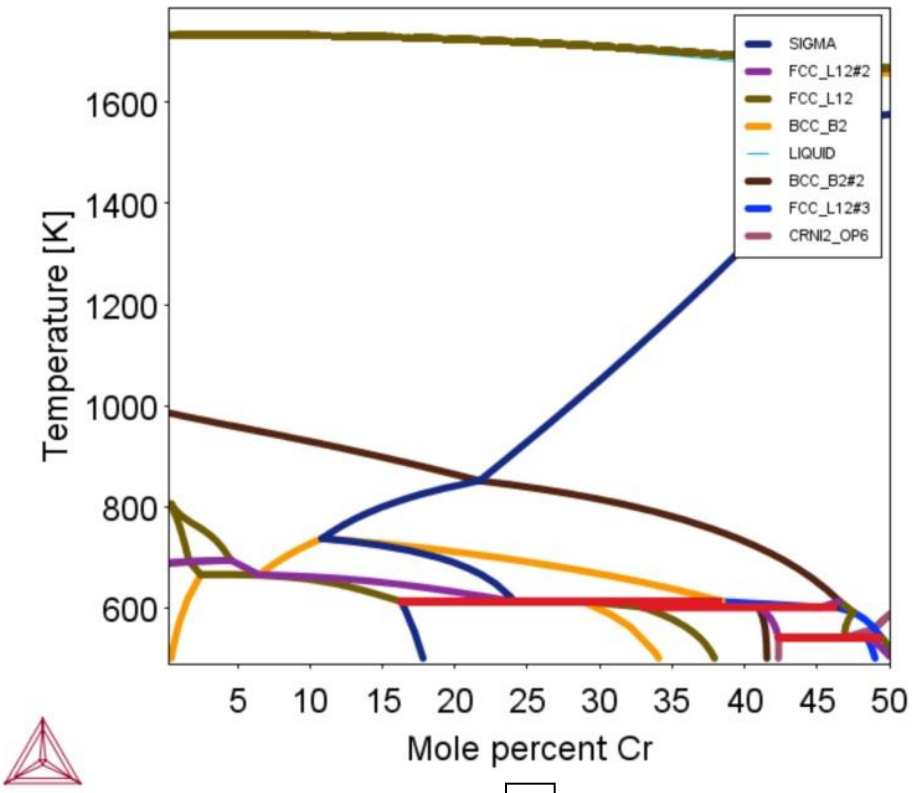
SIGMA
FCC_L12#2
FCC_L12
BCC_B2
LIQUID
BCC_B2#2
FCC_L12#3
CRNI2_OP6
Temperature [K]
1600
1400
1200
1000
800
600
5
10
15
20
25
30
35
40
45
50
Mole percent Cr

a

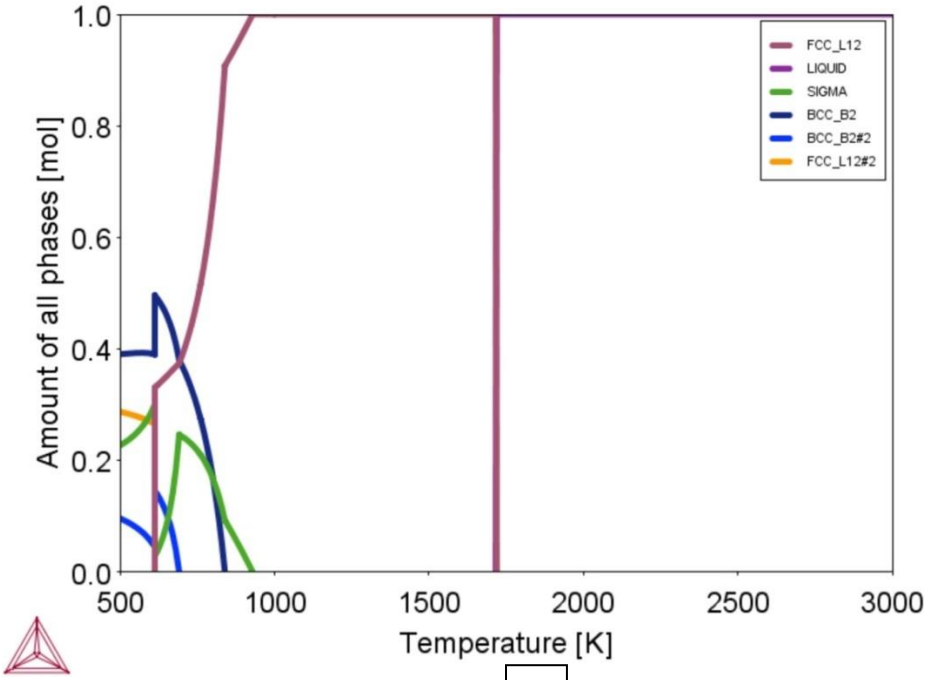
FCC_L12
LIQUID
SIGMA
BCC_B2
BCC_B2#2
FCC_L12#2
Amount of all phases [mol]
1.0
0.8
0.6
0.4
0.2
0.0
500
1000
1500
2000
2500
3000
Temperature [K]

b

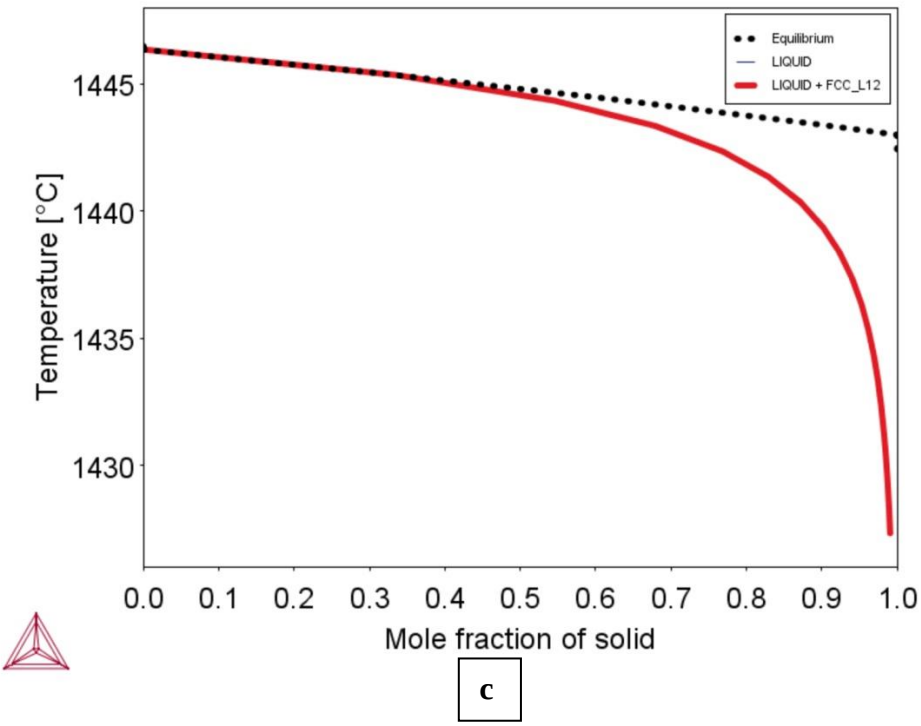

Fig. 5.1 a) Phase diagram b) Phase fraction Vs Temperature Phase diagram c) Solidification diagram of FeCoNiCr HEA

Thermocalc result for $FeCoNiCrZr_{10}$ system is shown in figure 2. Fig. 2a is the phase diagram of $FeCoNiCrZr_{10}$, showing that Zr = 10% is very close to eutectic point in which liquid gets solidified into three phases. At 1598K the liquid solidifies into FCC (L12), C15 laves phase and Ni_7Zr_2. The composition of the $FeCoNiCrZr_{10}$ is showed in Fig. 2b. The FCC (L12) phase is the major phase with about 0.6 mol fractions after that C15 laves phase comes forming about .3 mole fraction of our system while Ni_7Zr_2 has only 0.1 mole fractions in our system. Fig 2c shows us about way in which our system solidifies. Firstly liquid gets converted into FCC (L12) phase till 0.1 mole fraction of solid is formed after that it converts into C15 laves phase and FCC (L12) phase till we get 0.85 mole fraction of solid. Then after this we get FCC (L12), C15 laves and Ni_7Zr_2 till liquid gets completely solidified.

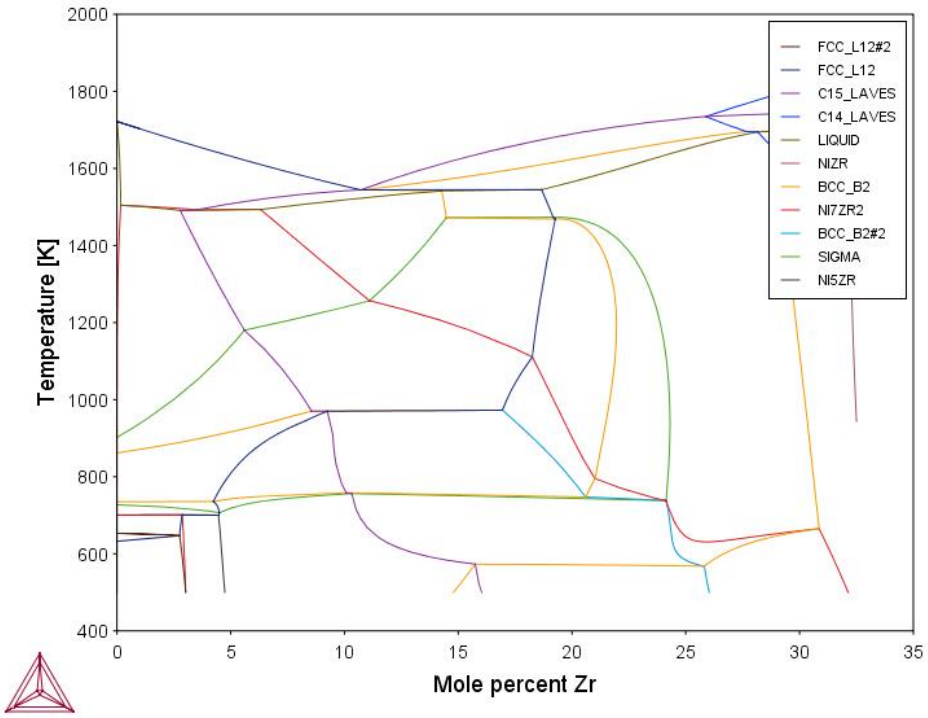
FCC_L12#2
FCC_L12
C15_LAVES
C14_LAVES
LIQUID
NIZR
BCC_B2
NI7ZR2
BCC_B2#2
SIGMA
NI5ZR
Temperature [K]
Mole percent Zr
2000
1800
1600
1400
1200
1000
800
600
400
0
5
10
15
20
25
30
35

a

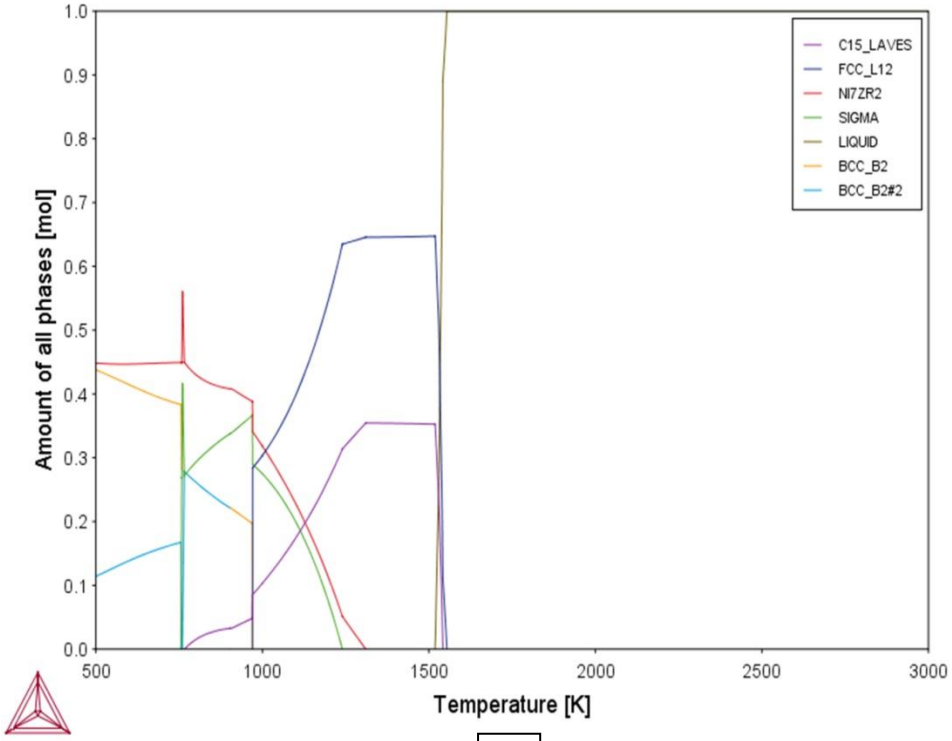
C15_LAVES
FCC_L12
NI7ZR2
SIGMA
LIQUID
BCC_B2
BCC_B2#2
Amount of all phases [mol]
Temperature [K]
1.0
0.9
0.8
0.7
0.6
0.5
0.4
0.3
0.2
0.1
0.0
500
1000
1500
2000
2500
3000

b

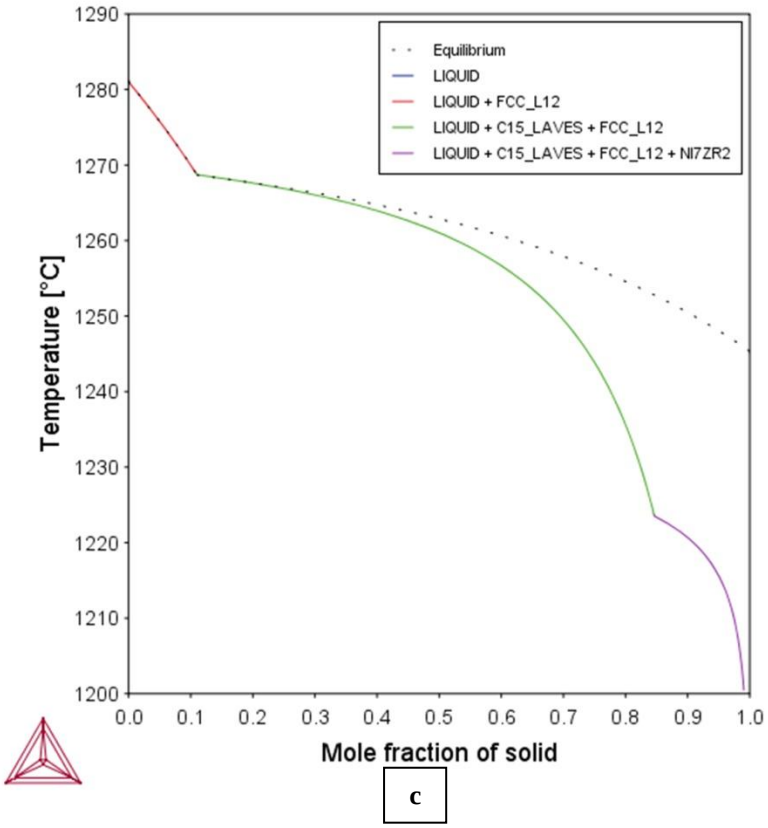

Fig.5. 2 a) Phase diagram b) Phase fraction Vs Temperature Phase diagram c) Solidification diagram of $FeCoNiCrZr_{10}$ HEA

Thermocalc result for FeCoNiCrAl is shown in Fig. 3. The phase diagram of Fig. 3a for FeCoNiCrAl shows hypereutectic system for Al = 20% in this some liquid gets converted into BCC (B2#2) phase then the remaining liquid gets converted into FCC (L12) phase. Figure 3b the solidification curve c for FeCoNiCrAl shows that first some liquid gets converted into BCC (B2#2) phase at 1700K then at 1598K the remaining liquid gets converted into BCC (B2) and FCC(L12) phase. The solidification pathway is shown in figure 3c in which about .9 mole fraction of liquid gets converted into BCC (B2#2) phase while remaining 0.1 mole fraction of liquid solidifies into BCC (B2) phase and FCC (L12) phase . The final composition of FeCoNiCrAl system is shown in fig. 3b. The BCC (B2#2) phase is the major phase while BCC (B2) and FCC (L12) are the minor phases. As the concentration of Al increases the FCC phase will decrease while the BCC phases will increase.

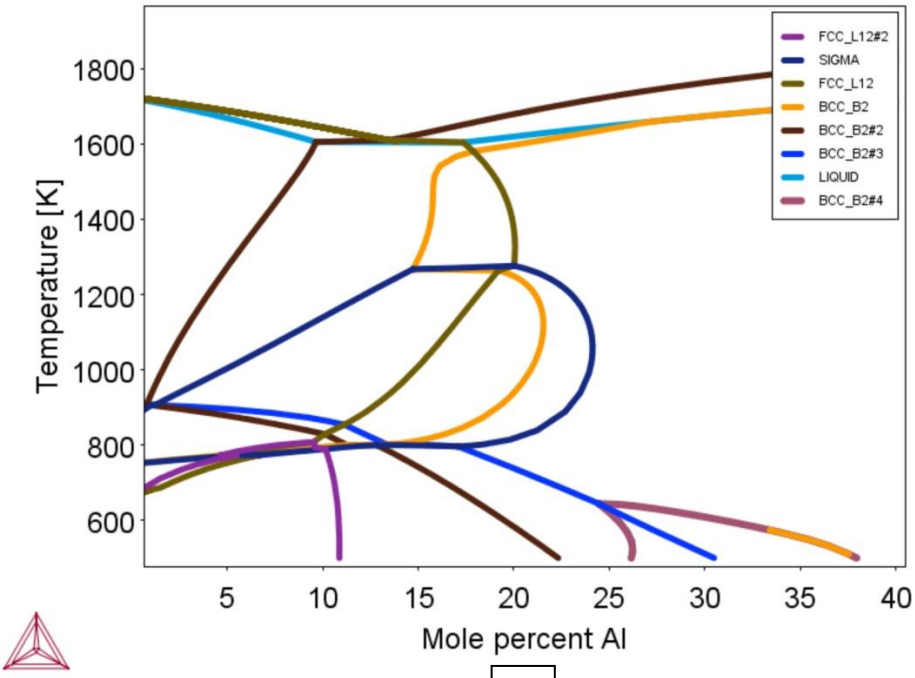
FCC_L12#2
SIGMA
FCC_L12
BCC_B2
BCC_B2#2
BCC_B2#3
LIQUID
BCC_B2#4
Temperature [K]
1800
1600
1400
1200
1000
800
600
5
10
15
20
25
30
35
40
Mole percent Al

a

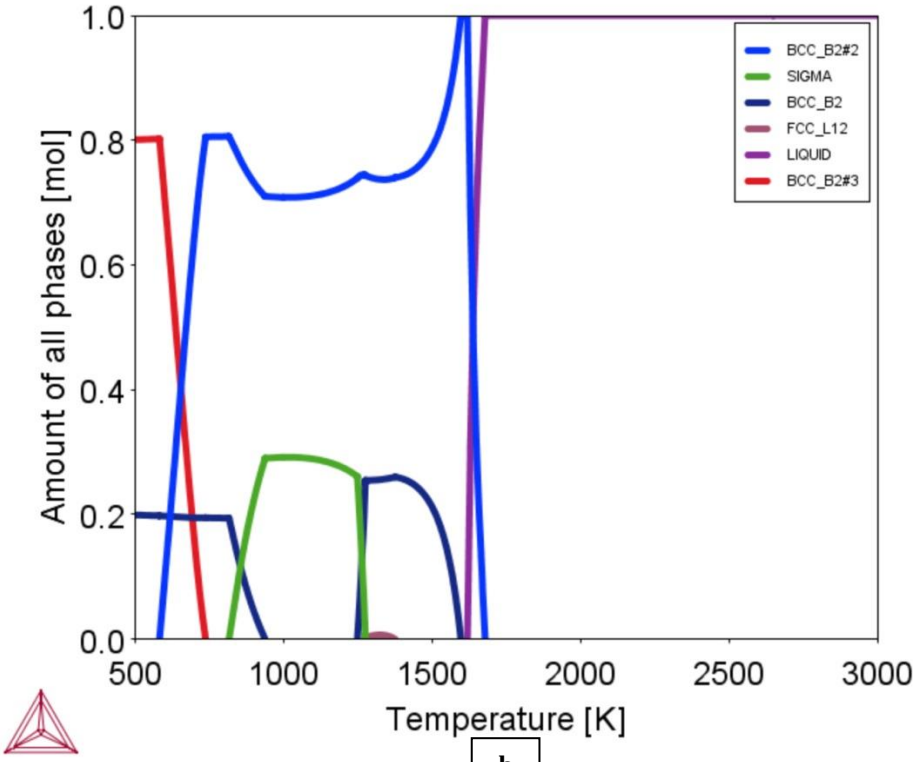
BCC_B2#2
SIGMA
BCC_B2
FCC_L12
LIQUID
BCC_B2#3
Amount of all phases [mol]
1.0
0.8
0.6
0.4
0.2
0.0
500
1000
1500
2000
2500
3000
Temperature [K]

b

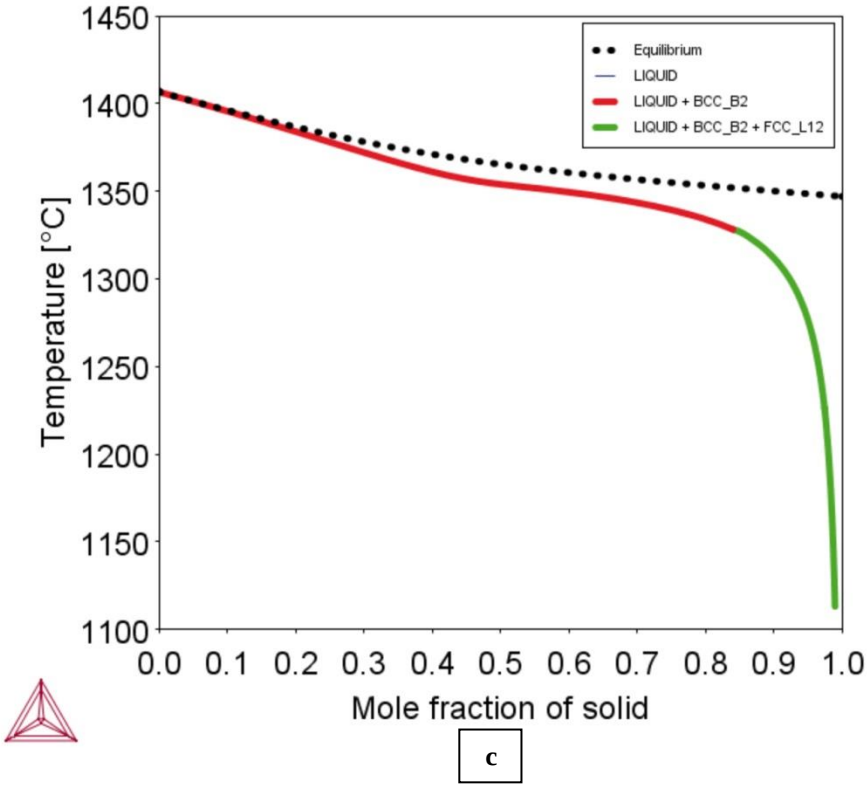

Fig. 5.3 a) Phase diagram b) Phase fraction Vs Temperature Phase diagram c) Solidification diagram of FeCoNiCrAl HEA

Themocalc results for $FeCoNiCrAlZr_{10}$ are shown in Fig. 4. The phase diagram for $FeCoNiCrAlZr_{10}$ is represented in fig. 4a showing that system is eutectic at 1600K temperature. Phase diagram suggest that after solidification BCC (B2), Hagg (HL21), Laves phase (C15), BCC (B2#2) and FCC(L12) phases gets evolved from the liquid system. The figure 4b is the solidification curve telling us about the composition of the $FeCoNiCrAlZr_{10}$ at various temperatures. From the solidification curve we can say that the BCC (B2) phase is the dominant phase while other phases are minor phases.

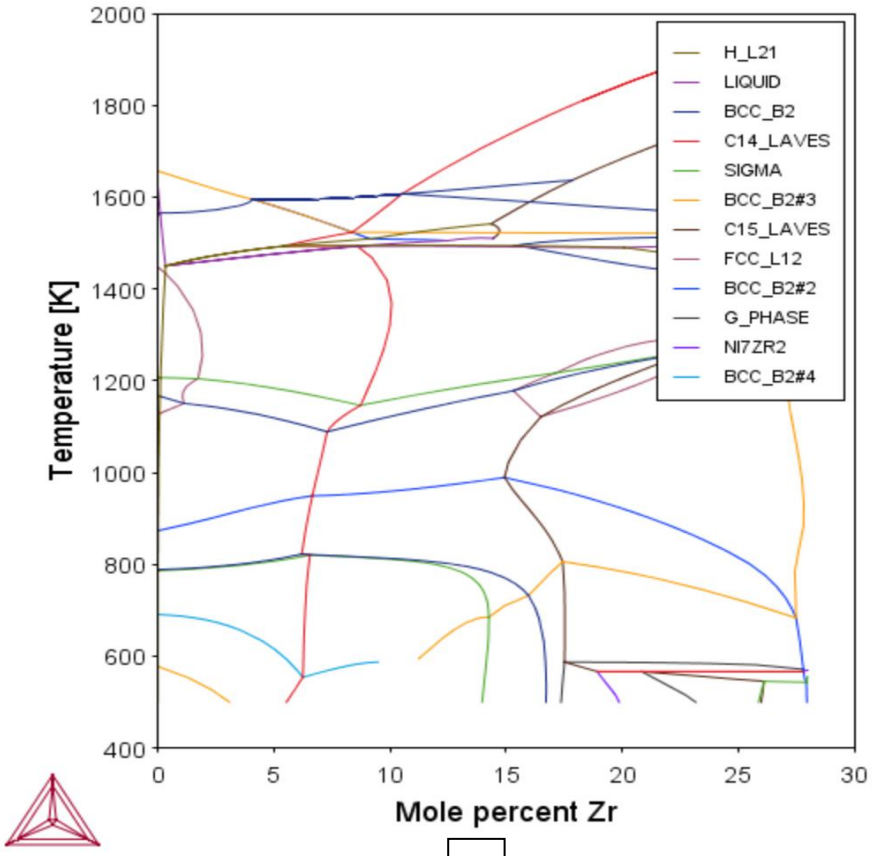
H_L21
LIQUID
BCC_B2
C14_LAVES
SIGMA
BCC_B2#3
C15_LAVES
FCC_L12
BCC_B2#2
G_PHASE
NI7ZR2
BCC_B2#4
Temperature [K]
Mole percent Zr
2000
1800
1600
1400
1200
1000
800
600
400
0
5
10
15
20
25
30

a

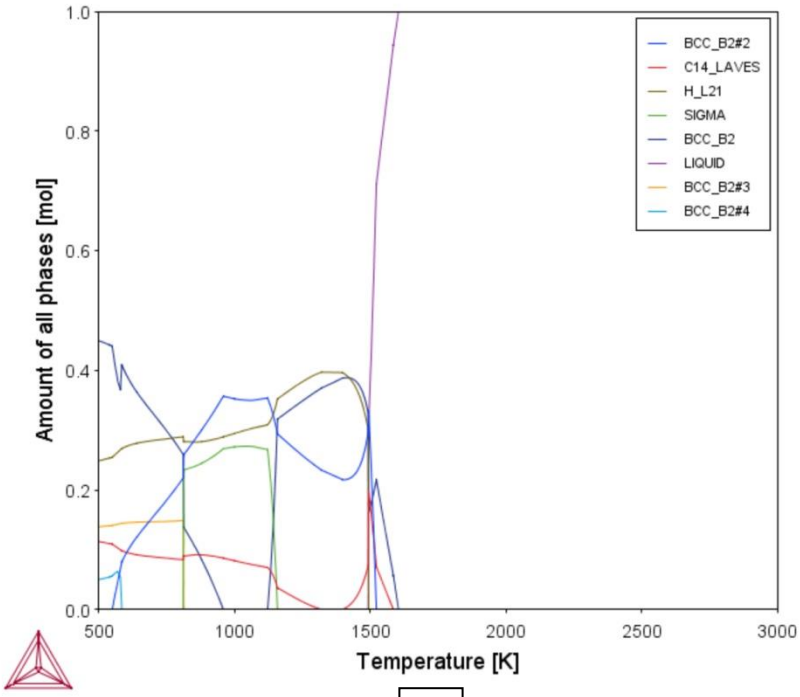
BCC_B2#2
C14_LAVES
H_L21
SIGMA
BCC_B2
LIQUID
BCC_B2#3
BCC_B2#4
Amount of all phases [mol]
Temperature [K]
1.0
0.8
0.6
0.4
0.2
0.0
500
1000
1500
2000
2500
3000

b

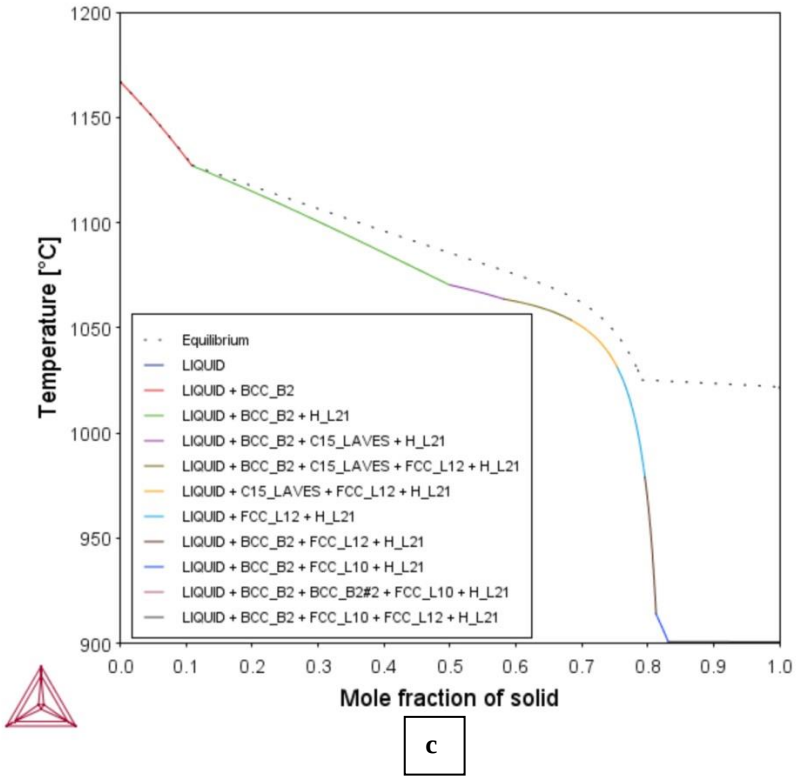

Fig. 5.4 a) Phase diagram b) Phase fraction Vs Temperature Phase diagram c) Solidification diagram of $FeCoNiCrAlZr_{10}$HEA

Thermocalc result for the $FeCoNiCrCuZr_{10}$ is shown in fig. 5. The phase diagram for $FeCoNiCuZr_x$ is represented in fig. 5a shows eutectic point at about 1450K temperature and mole percentage of 8%. So $FeCoNiCrCuZr_{10}$ is a hyper eutectoid system having mixture of eutectic and dendritic phases. Solidification curve fig. 5c suggest during solidification Laves phase (C15), FCC phase (L12&L10) and intermetallic of Ni_7Zr_2 will be formed. The figure 5b is the solidification curve telling us about the composition of the $FeCoNiCrCuZr_{10}$ at various temperatures. From the solidification curve we can say that the FCC (L10&L12) phases are the dominant phases while other phases are minor phases.

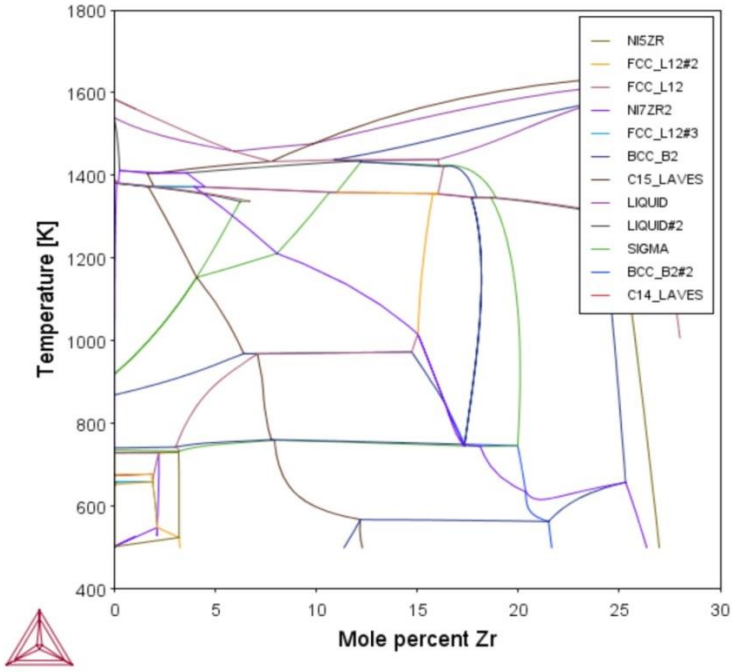
Temperature [K]
Mole percent Zr
NI5ZR
FCC_L12#2
FCC_L12
NI7ZR2
FCC_L12#3
BCC_B2
C15_LAVES
LIQUID
LIQUID#2
SIGMA
BCC_B2#2
C14_LAVES

a

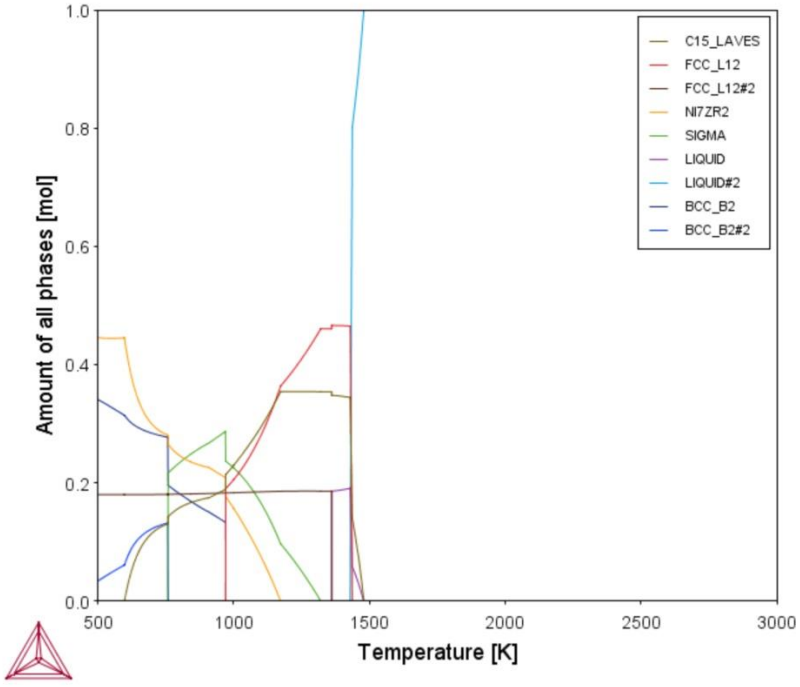
Amount of all phases [mol]
Temperature [K]
C15_LAVES
FCC_L12
FCC_L12#2
NI7ZR2
SIGMA
LIQUID
LIQUID#2
BCC_B2
BCC_B2#2

b

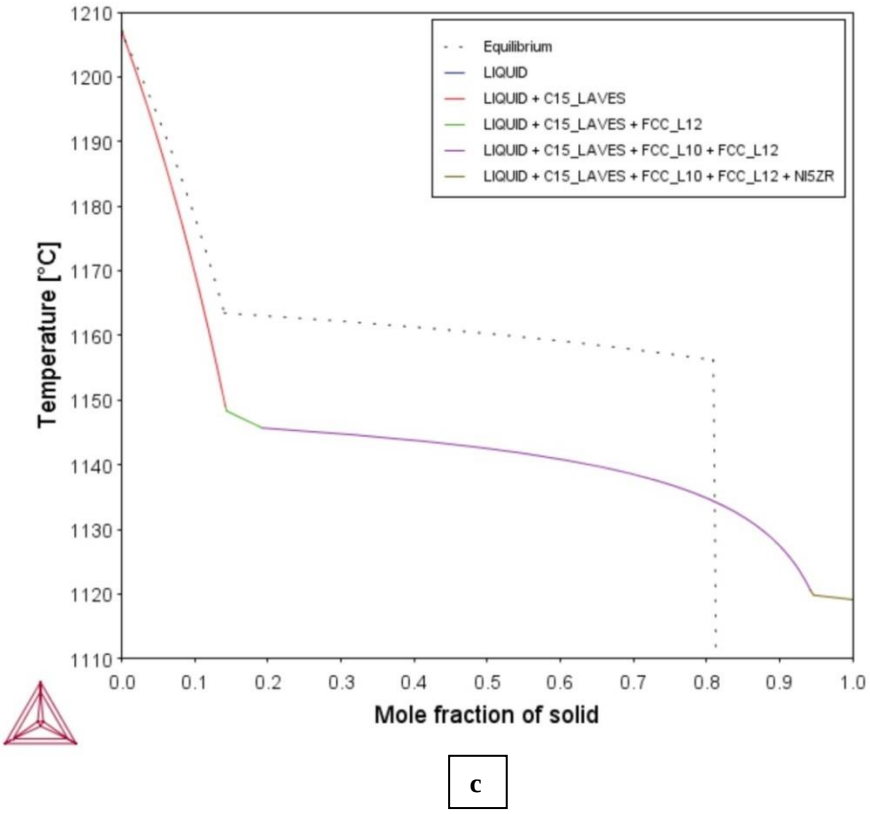

Fig.5.5 a)Phase diagram b) Phase fraction Vs Temperature Phase diagram c) Solidification diagram of $FeCoNiCrCuZr_{10}$ HEA

Chapter 6

Results and Discussion

6.1 Parameters Calculation for design of high entropy alloys

Thermodynamic and Hume-Rothery parameters for $FeCoNiCrZr_x$ HEAs were calculated. There values were exhibited in Table 1. The ΔG_{mix} is lowering, forming stable phases at room temperature. Increase in Zr content leading to increase in value of ΔH_{mix} showing evolution of intermetallics in the alloy. The value of ΔS_{mix} is also increasing with the increase of Zr content. As we know that increase in mixing enthalpy (ΔH_{mix}) will lead to formation ordered intermetallics, while on other hand increase in mixing entropy will lead to evolution of disordered solid solution phases. Therefore, to compare the effect of both parameters we use Ω to determine the phases involved in HEA. As in case of FeCoNiCr Ω is very large, the mixing entropy is predominant our enthalpy thus there is a formation of single solid solution phase. But as the Zr content raise the value of Ω decreases reveals the effect of mixing enthalpy is rising faster as compared to entropy, thus showing increase in the formation of intermetallics phases in the HEAs. Similarly the melting temperature calculated through mixture rule for $FeCoNiCrZr_x$ HEA system also increases with the rise of Zr content. The atomic size difference (δ) for FeCoNiCr is very low showing formation of solid solution phases. As value of atomic size difference (δ) increase with rise in Zr content showing evolution of intermetallics along with decrease in solid solution phase. The valence electron concentration (VEC) value of $FeCoNiCrZr_x$ HEA system is around to 8 showing formation of face centered solid solution. The value of electronegativity difference (Δ□) for FeCoNiCr system is very low shows evolution of single solid solution phase. While the increase in Zr content leads to increase in electronegativity difference (Δ□) revealing the formation of intermetallics. To combine the effect of

mixing entropy (ΔS_{mix}) and atomic size difference (δ) a new parameter Λ is introduced. The value of Λ for FeCoNiCr is very large reveals that mixing entropy (ΔS_{mix}) is predominant over atomic size difference (δ) factor thus there is evolution of single solid solution phase. But due to addition of Zr the value of Λ decreases causing evolution of eutectic structure having solid solution phase along with intermetallics.

Table 6.1

a) Thermodynamic Parameters

Alloy	ΔH_{mix}	ΔS_{mix}	ΔG_{mix}	T_m (K)
FeCoNiCr	-3.75	11.525	-7.210	1858
$FeCoNiCrZr_{2.5}$	-6.66	12.209	-10.323	1864.67
$FeCoNiCrZr_5$	-9.42	12.6	-13.2	1871.35
$FeCoNiCrZr_{7.5}$	-12.0	12.876	-15.883	1878.02
$FeCoNiCrZr_{10}$	-14.47	13.075	-18.39	1884.7

b) Hume-Rothery factors

Alloy	Ω	δ(%)	VEC	Δ□	Λ
FeCoNiCr	5.71	.3	8.25	0.097	128.05
$FeCoNiCrZr_{2.5}$	3.42	4.44	8.143	.122	.619
$FeCoNiCrZr_5$	2.5	6.15	8.037	.142	.333
$FeCoNiCrZr_{7.5}$	2.02	7.37	7.931	.160	.237
$FeCoNiCrZr_{10}$	1.7	8.34	7.825	.234	.1879

For $FeCoNiCrAlZr_x$ HEAs the trend in ΔG_{mix}, ΔH_{mix} and ΔS_{mix} values are similar to the result of $FeCoNiCrZr_x$ HEA as shown in table 2.Therefore in case of FeCoNiAlCr Ω is more than one, the mixing entropy is predominant our enthalpy thus there is a formation of solid solution phase. But as the Zr content raise the value of Ω decreases reveals the effect of

mixing enthalpy is rising faster as compared to entropy, thus showing increase in the formation of intermetallics phases in the HEAs. Similarly the melting temperature calculated through mixture rule for $FeCoNiCrAlZr_x$ HEA system also increases with the rise of Zr content. The atomic size difference (δ) for FeCoNiCrAl is less than 6.6%, showing formation of stable solid solution phases. As value of atomic size difference (δ) for $FeCoNiCrAlZr_x$ (X = 2.5,5.0,7.5,10.0) is more than 6.6%, reveals that rise in Zr content causes evolution of intermetallics along with decrease in solid solution phase. The valence electron concentration (VEC) value of $FeCoNiCrAlZr_x$ HEA system is in between 6.87 to 8 showing formation of body centered and face centered solid solution. The value of electronegativity difference (Δ□) for FeCoNiCrAl system is less shows evolution of stable solid solution phase with intermetallics. While the increase in Zr content leads to increase in electronegativity difference (Δ□) revealing the formation of intermetallics. To combine the effect of mixing entropy (ΔS_{mix}) and atomic size difference (δ) a new parameter Λ is introduced. The value of Λ for FeCoNiCrAl is very large reveals that mixing entropy (ΔS_{mix}) is predominant over atomic size difference (δ) factor thus there is evolution of stable solid solution phase along with some intermetallics. But due to addition of Zr the value of Λ decreases causing evolution of eutectic structure having solid solution phase along with intermetallics

Table 6.2

Thermodynamic Parameters

Alloy	ΔH_{mix}	ΔS_{mix}	ΔG_{mix}	T_m (K)
FeCoNiCrAl	-12.32	13.38	-16.33	1673.1
$FeCoNiCrAlZr_{2.5}$	-15.046	14.02	-19.252	1684.52
$FeCoNiCrAlZr_5$	-17.616	14.362	-21.925	1695.7
$FeCoNiCrAlZr_{7.5}$	-20.032	14.60	-24.412	1706.98
$FeCoNiCrAlZr_{10}$	-22.30	14.75	-26.725	1718.30

Hume – Rothery factors

Alloy	Ω	δ(%)	VEC	Δ□	Λ
FeCoNiCrAl	1.817	5.72	7.2	.121	.408
$FeCoNiCrAlZr_{2.5}$	1.57	6.85	7.12	.1381	.298
$FeCoNiCrAlZr_{5}$	1.382	7.72	7.04	.1527	.241
$FeCoNiCrAlZr_{7.5}$	1.244	8.43	6.96	0.1654	.205
$FeCoNiCrAlZr_{10}$	1.136	9.032	6.88	0.1765	0.181

Thermodynamic and Hume Rothery factors for $FeCoNiCrCuZr_x$ HEA were calculated to analyze the morphology of the alloy system. The calculated values for this system are shown in Table 3. The trend for ΔG_{mix} values for this system is negative showing formation of stable phases. Similarly, ΔH_{mix} value is between 5 to -15 KJ/mol showing formation of solid solution. High value ΔS_{mix} also shows formation of stable solid solution.. Therefore, to compare the effect of both parameters we use Ω to determine the phases involved in HEA. As in case of FeCoNiCuCr Ω is more than one, the mixing entropy is predominant our enthalpy thus there is a formation of solid solution phase. But as the Zr content increases the value of Ω decreases reveals the effect of mixing enthalpy is rising faster as compared to entropy, thus showing increase in the formation of intermetallics phases in the HEAs. Similarly the melting temperature calculated through mixture rule for $FeCoNiCrAlZr_x$ HEA system also increases with the rise of Zr content. The atomic size difference (δ) for FeCoNiCrAl is less than 6.6%, showing formation of stable solid solution phases. As value of atomic size difference (δ) for $feCoNiCrAlZr_x$ (X = 2.5,5.0,7.5,10.0) is increasing, reveals that rise in Zr content causes evolution of intermetallics along with decrease in solid solution phase. The valence electron concentration (VEC) value of $FeCoNiCrCuZr_x$ HEA system is more than 8, showing formation of face

centered solid solution. The value of electronegativity difference (Δ□) for FeCoNiCrCu system is very less shows evolution of stable solid solution phase. While the increase in Zr content leads to increase in electronegativity difference (Δ□) revealing the formation of intermetallics. To combine the effect of mixing entropy (ΔS_{mix}) and atomic size difference (δ) a new parameter Λ is introduced. The value of Λ for FeCoNiCrCu is very large reveals that mixing entropy (ΔS_{mix}) is predominant over atomic size difference (δ) factor thus there is evolution of stable solid solution phase along with some intermetallics. But due to addition of Zr the value of Λ decreases causing evolution of eutectic structure having solid solution phase along with intermetallics

Table 6.3

Thermodynamic Parameters

Alloy	ΔH_{mix}	ΔS_{mix}	ΔG_{mix}	T_m (K)
FeCoNiCrCu	3.20	13.38	-0.814	1757.95
$FeCoNiCrCuZr_{2.5}$	0.117	14.02	-4.089	1767.13
$FeCoNiCrCuZr_5$	-2.812	14.362	-7.121	1776.31
$FeCoNiCrCuZr_{7.5}$	-5.587	14.60	-9.967	1785.5
$FeCoNiCrCuZr_{10}$	-8.208	14.75	-12.633	1794.66

Hume – Rothery Factors

Alloy	Ω	δ(%)	VEC	Δ□	Λ
FeCoNiCrCu	7.35	1.033	8.8	.092	12.54
$FeCoNiCrCuZr_{2.5}$	211.75	4.45	8.68	0.12	0.71
$FeCoNiCrCuZr_5$	9.07	6.08	8.56	0.14	0.39
$FeCoNiCrCuZr_{7.5}$	4.66	7.27	8.44	0.16	0.276
$FeCoNiCrCuZr_{10}$	3.225	8.21	8.21	0.17	0.22

6.2 Characterization of HEAs synthesized through Solidification route

To evaluate the phases and structure of our samples various microstructural analysis techniques like XRD, SEM are used. The results obtained by this technique are shown in this chapter.

6.2.1 Structural Characterization

The x-ray diffraction (XRD) pattern of $FeCoNiCrZr_x$ (X= 0, 2.5, 5.0, 7.5, 10) is shown in fig. 6.1. It is found that the XRD pattern of FeCoNiCr alloy reveals the diffraction peaks corresponding to only FCC phase. While the XRD patterns of $FeCoNiCrZr_x$ (X= 2.5, 5.0, 7.5, 10) show the diffraction peaks corresponding to FCC solid solution phase and Laves phase. It is to be noted that the Laves phase is observed to form with the addition of Zr in the base FeCoNiCr alloy and also the amount of Laves phase increases with the increase of Zr concentration.

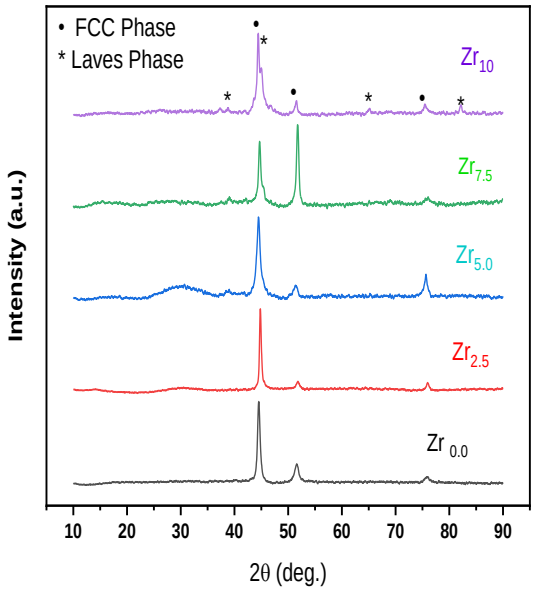

Fig 6.1 XRD of $FeCoNiCrZr_x$ (X= 0, 2.5, 5.0, 7.5, 10) samples

Fig. 6.2 shows XRD pattern of $FeCoNiCrAlZr_x$ (X= 0, 2.5, 5.0, 7.5, 10) HEAs.

The XRD pattern reveals the presence of BCC phase and Laves phase. The addition of Al in FeCoNiCr leads to the formation of a BCC solid solution phase. The addition of zirconium in FeCoNiCrAl will lead to the development of Laves phase. As the zirconium contain increases, the amount of Laves phase in $FeCoNiCrAlZr_x$ also increases.

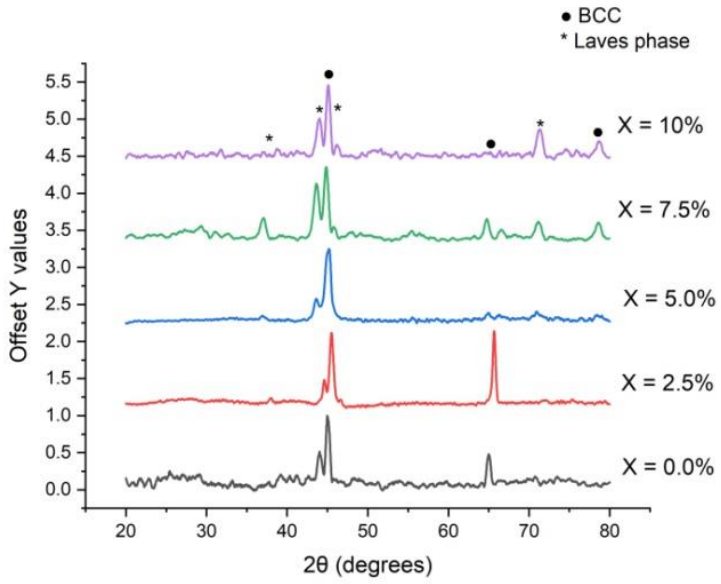

Fig. 6.2 XRD pattern of $FeCoNiCrAlZr_x$ (X= 0, 2.5, 5.0, 7.5, 10) sample.

The x-ray diffraction pattern of $FeCoNiCrCuZr_x$ (X= 0, 2.5, 5.0, 7.5, 10) is given in Fig. 6.3. The addition of Cu in FeCoNiCr leads to the transformation of single fcc solid solution phase into two fcc solid solution phases. The XRD pattern of FeCoNiCrCu HEA shows the formation of two fcc solid solution phases; first is matrix of solid solution while other is ordered Cu-rich phase. The addition of Zr leads to the formation of Laves phases.

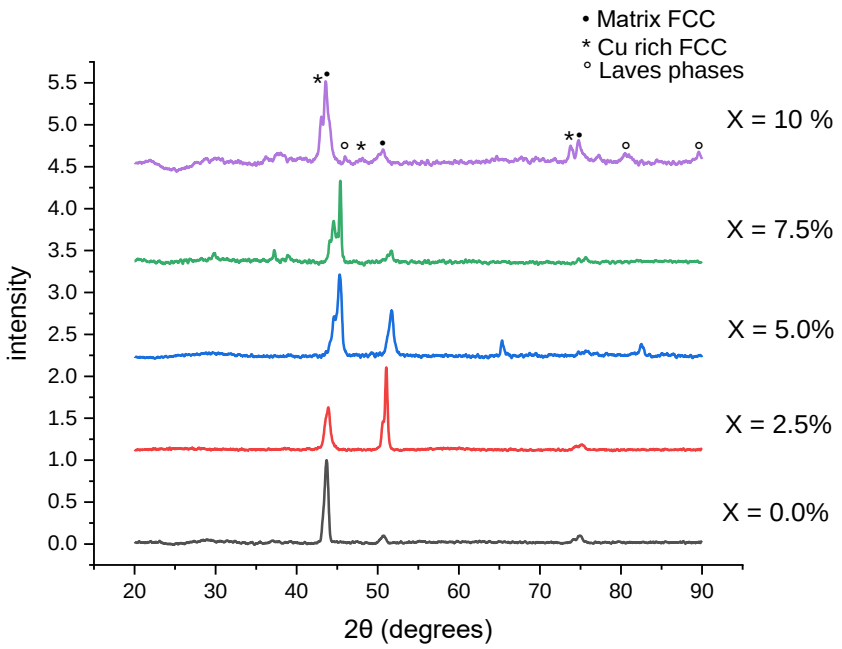

Fig. 6.3 XRD pattern of $FeCoNiCrCuZr_x$ (X= 0, 2.5, 5.0, 7.5, 10) samples

6.2.2 Microstructural characterization

The optical micrograph of $FeCoNiCrZr_x$ (X= 0, 2.5, 5.0, 7.5, 10) are shown in fig. 6.4. The optical micrograph determines the surface morphology of the samples. Fig. 6.4a shows the optical image of FeCoNiCr having a plane morphology suggesting presence of single phase. Fig. 6.4b shows an optical micrograph of hypoeutectic $FeCoNiCrZr_{2.5}$ sample. This micrograph shows small amount of eutectic morphology along with some columnar dendritic microstructure. In fig. 6.4e, the optical micrograph shows the hypoeutectic $FeCoNiCrZr_{10}$ sample having two types of eutectics. First one is lamellar eutectic while second one is globular eutectic having predominant dendritic microstructure. It is observed from Fig. 6.4a to 6.4e that the volume fraction of eutectic morphology increases with increase of Zr concentration.

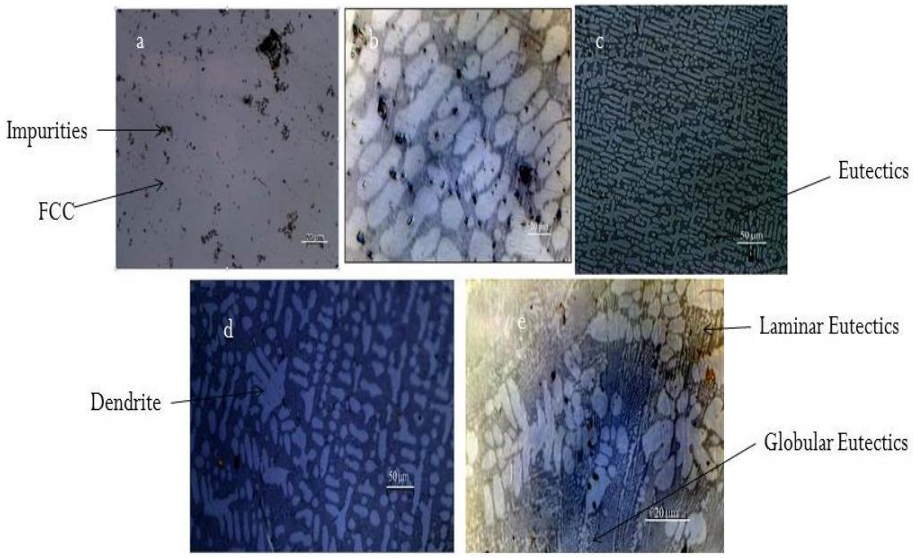

Fig. 6.4 Optical Micrograph of $FeCoNiCrZr_x$(X = 0, 2.5, 5.0, 7.5, 10.0)

The optical micrograph for $FeCoNiCrAlZr_x$ (X = 0.0, 2.5, 5.0, 7.5, 10) is represented in fig. 6.5. The optical image of FeCoNiCrAl is shown in fig. 6.5a. The optical micrograph shows the equiaxed-dendrite morphology having fine-scale structure with alternating bright and dark interconnected phases. In fig. 6.5b, the optical micrograph of $FeCoNiCrAlZr_{2.5}$ reveals the eutectic morphology along with non-equiaxed dendritic microstructure. Due to the addition of Zr in FeCoNiCrAl system, the evolution of eutectic morphology develops(as shown in the micrograph). From fig. 6.5b to 6.5e,it is observed that as the concentration of Zr increases, the volume fraction of eutectics also increases along with evolution non-equiaxed dendritic microstructure.

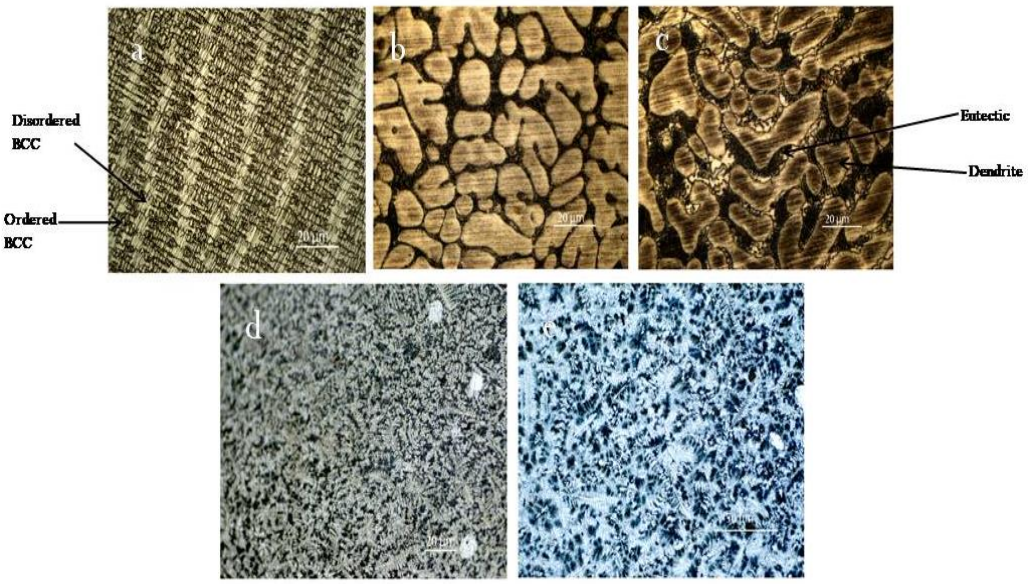

Fig. 6.5 Optical micrograph of $FeCoNiCrAlZr_x$(X=0, 2.5, 5, 7.5, 10)

The optical micrograph of $FeCoNiCrCuZr_x$ (X = 0.0, 2.5, 5.0, 7.5, 10.0) are shown in fig. 6.6. In fig. 6.6a, optical micrograph of $FeCoNiCrCuZr_{2.5}$ shows the columnar dendritic microstructure. The alternating dark and bright phases in interdendritic region are signature of eutectic microstructure. It is to be noted that the alloy is transformed from two phase fcc solid solution phases to eutectic morphology due to addition of zirconium. In fig. 6.6 a to c, it is also seen that the volume fraction eutectics increases due to increase of Zr content. Fig. 6.6d shows the optical image of $FeCoNiCrCuZr_{10}$ which consists of large amount of needle shape dark phase along with eutectic microstructure. It is found that $FeCoNiCrCuZr_{7.5}$ (as shown in fig. 6.6c) is nearly eutectic HEA with minute fraction of dendritic phases.

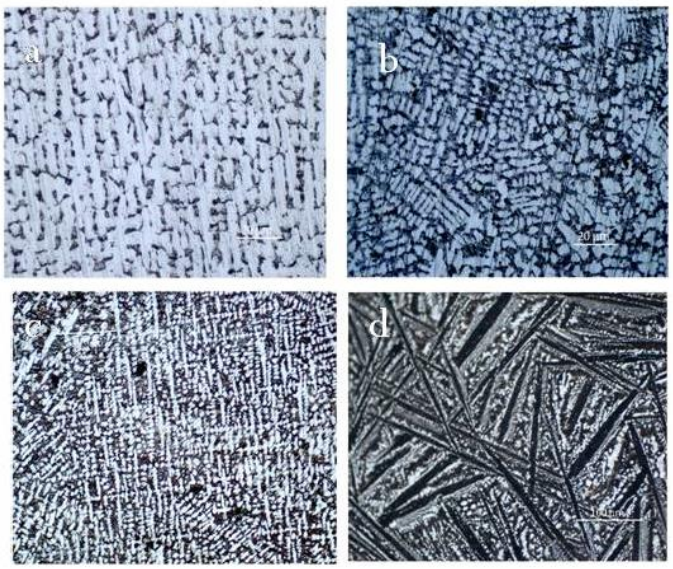

Fig. 6.6 Optical micrograph of $FeCoNiCrCuZr_x$ (X = 2.5, 5.0, 7.5, 10.0)

Field emission scanning electron microscopy was used for microstructural characterization of the designed HEAs. The backscattered electron (BSE) mode of SEM is used to distinguish the different phases in microstructure of HEAs due to Z-contrast. The SEM images at low magnification for $FeCoNiCrZr_x$ (X= 0, 7.5, 10) alloy system in BSE mode are represented in fig.6.7 while high magnification SEM images for systems are shown in fig. 6.8.

Fig. 6.7a and 6.8a exhibits single phase face centered solid solution morphology of FeCoNiCr. While fig. 6.7b and 6.8b exhibits a typical hypoeutectic morphology for $FeCoNiCrZr_{7.5}$. $FeCoNiCrZr_{7.5}$ alloy system consists of dendrite face centered solid solution phase along with eutectic phase (as shown in fig. 6.7b). The eutectic phase has lamellar morphology, which consists of mixture of face centered solid solution phase and Laves phase. Fig 6.7c exhibits fully eutectic morphology for $FeCoNiCrZr_{10}$ HEA. Fig. 6.8c reveals a bimodal eutectic system for $FeCoNiCrZr_{10}$ HEA. First is lamellar eutectic phase which consists of mixture of face centred solid solution and Laves phase. Second one is globular eutectics consisting of mixture of face centered solid solution and intermetallics.

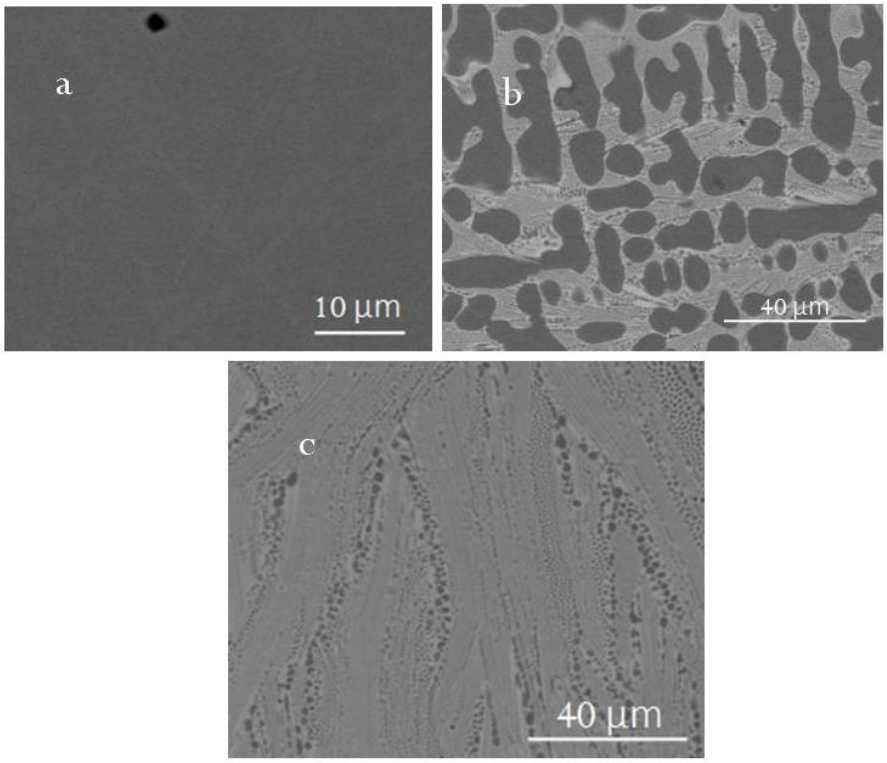

Fig. 6.7 Low magnification SEM images of $FeCoNiCrZr_x$ (0, 7.5, 10)

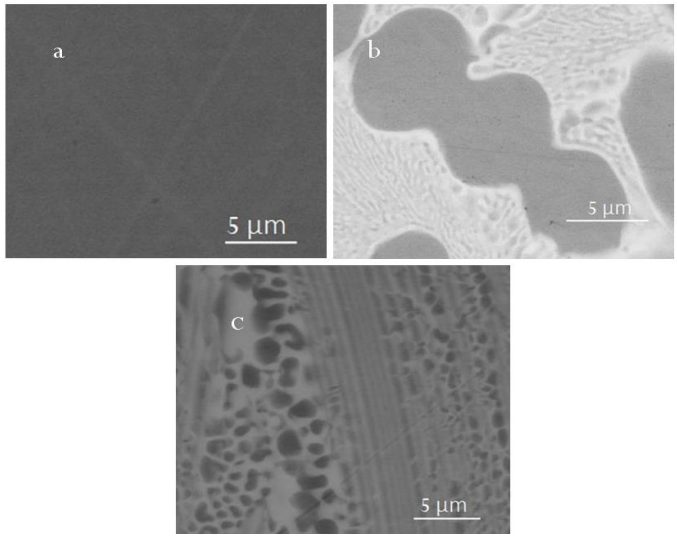

Fig. 6.8 High magnification SEM images of $FeCoNiCrZr_x$ (X = 0, 7.5, 10)

The Energy-dispersive X-ray spectroscopy (EDS) for $FeCoNiCrZr_{7.5}$ and $FeCoNiCrZr_{10}$ is shown in fig. 6.9 and 6.10, respectively. Fig. 6.9a for $FeCoNiCrZr_{7.5}$ exhibits darker phase is Zr deficient. While fig. 6.9b

exhibits that brighter phase is rich in Zr. The elemental analysis of both the phase for $FeCoNiCrZr_{7.5}$ is given in Table 3. The EDS for the $FeCoNiCrZr_{10}$ HEA (fig. 6.10) reveals that brighter phase is very rich in Zr along with other elements. The elemental composition analysis for brighter phase of $FeCoNiCrZr_{10}$ HEA is given in Table 4. The elemental analysis of both the phase for $FeCoNiCrZr_{10}$ is given in Table 4.

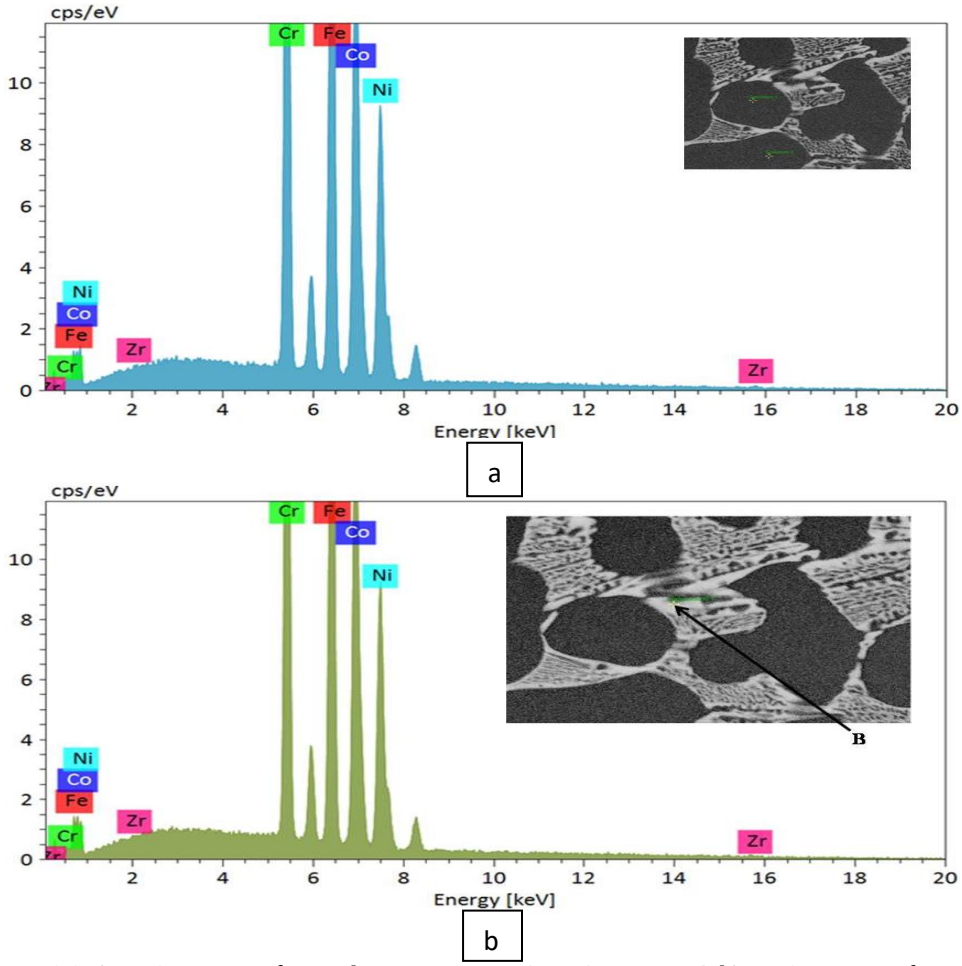

Fig. 6.9 a) EDS mapping for Darker region in $FeCoNiCrZr_{7.5}$ HEA b) EDS mapping for brighter region in $FeCoNiCrZr_{7.5}$ HEA

Table 6.4

Elements	Fe (at. %)	Co (at. %)	Ni (at. %)	Cr (at. %)	Zr (at. %)
Darker region	31.25	25.58	24.73	17.65	0.79
Brighter region	21.15	24.19	26.90	16.31	11.45

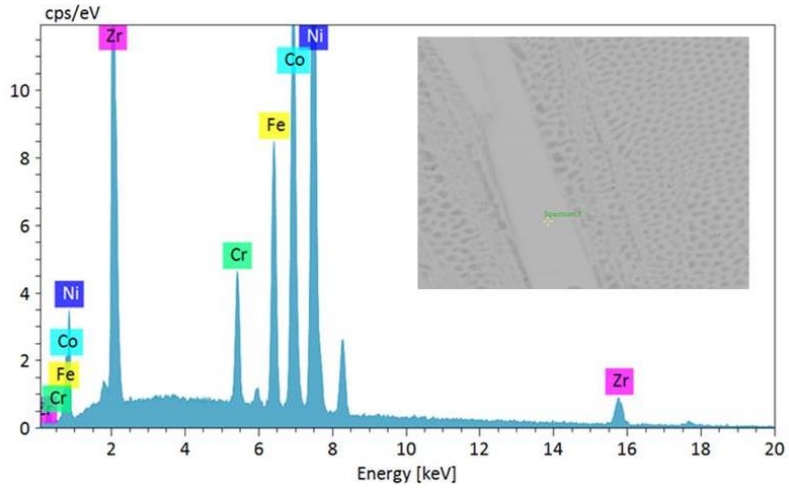

Fig. 6.10 EDS mapping of brighter region of $FeCoNiCrZr_{10}$ HEA

Table 6.5

Elements	Fe	Co	Ni	Cr	Zr
Atomic percent (%)	12.98	24.80	38.14	5.07	19.01

The FESEM images at for $FeCoNiCrCuZr_x$ (X= 2.5, 5.0, 7.5, 10) alloy system in BSE mode are shown in fig.6.11.

Fig. 6.11a exhibits hypoeutectic morphology for $FeCoNiCrCuZr_{2.5}$ HEA system. $FeCoNiCrCuZr_{2.5}$ HEA consists of two different types of face centered solid solution phases with dendritic morphology. Fig. 6.11b exhibits increase in eutectic region along with dendritic morphology in

$FeCoNiCrCuZr_{5.0}$. $FeCoNiCrCuZr_{7.5}$ HEA (as shown in fig. 6.11c) reveals a fine eutectic morphology consist of finely spread intermetallics into face centered solid solution. $FeCoNiCrCuZr_{10}$ (as shown in Fig. 6.11d) reveals the hypereutectic morphology consisting of dendrite and interdendritic eutectic morphology.

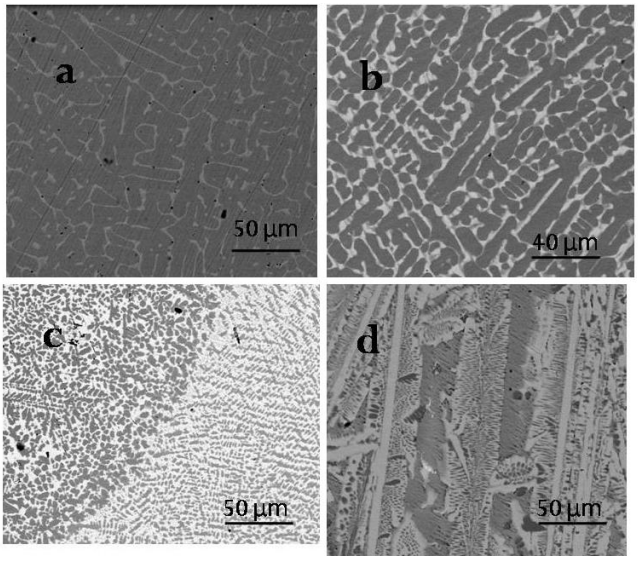

Fig 6.11 SEM images in BSE mode for $FeCoNiCrCuZr_x$ (x = 2.5, 5.0, 7.5, 10)

The EDS mapping of $FeCoNiCrCuZr_x$ (x = 2.5, 5.0, 7.5, 10) is shown in fig. 6.12, 6.13, 6.14 and 6.15, respectively.

$FeCoNiCrCuZr_{2.5}$ consists of two face centered solid solution phases along with some eutectic region. Brighter region (spectrum 1) is copper rich solid solution phase while darker region (spectrum 2) is FeCoNiCr rich solid solution phase as shown in fig. 6.12. The elemental analysis of the $FeCoNiCrCuZr_{2.5}$ HEA is given in Table 5.

The EDS analysis of $FeCoNiCrCuZr_{5.0}$ HEA is done to determine the composition of phases in the microstructure (as shown in fig. 6.13). The elemental analysis of the $FeCoNiCrCuZr_{5.0}$ HEA is given in Table 6.

EDS mapping of $FeCoNiCrCuZr_{7.5}$ is done at four points to determine the composition of constituent phases in the microstructure (as shown in fig.

6.14).The elemental analysis of the $FeCoNiCrCuZr_{7.5}$ HEA is given in Table 7.

EDS mapping of $FeCoNiCrCuZr_{10}$ is done at four points to determine the composition of phases as shown in fig. 6.15.The elemental analysis of the $FeCoNiCrCuZr_{10}$ HEA is given in Table 8.

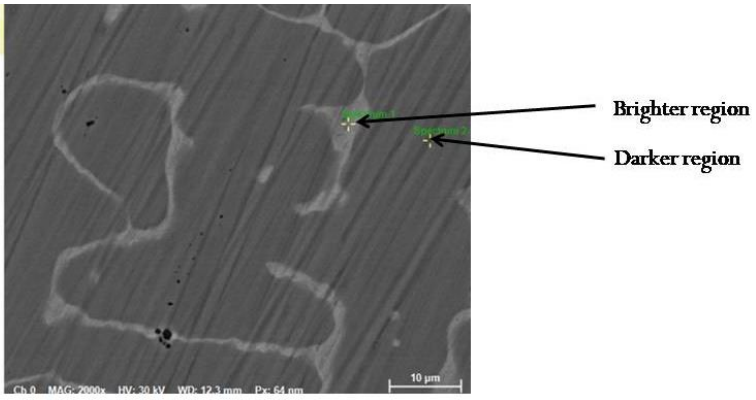

Fig. 6.12 EDS mapping of $FeCoNiCrCuZr_{2.5}$

Table 6.6

Element	Fe	Co	Ni	Cr	Cu	Zr
Brighter	4.92	4.79	8.67	2.91	78.69	0.01
Darker	24.3	23.63	22.56	16.76	12.49	0.25

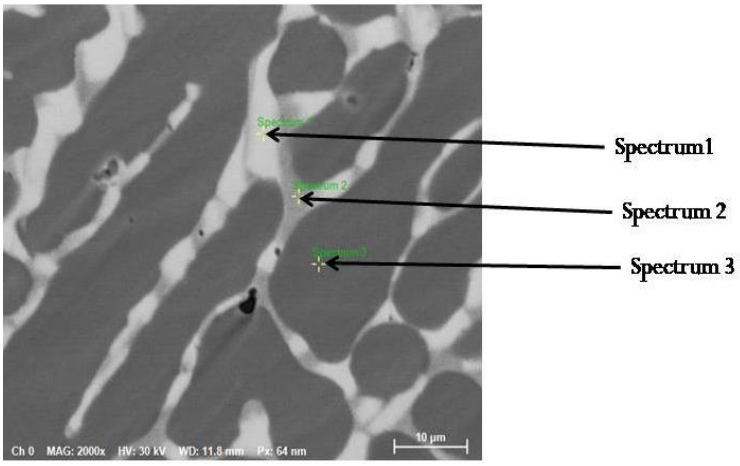

Fig. 6.13 . EDS mapping of $FeCoNiCrCuZr_{5.0}$

Table 6.7

Element	Fe	Co	Ni	Cr	Cu	Zr
Spect.1	7.57	15.49	38.22	4.07	18.45	16.21
Spect.2	3.17	3.16	6.80	2.13	84.45	0.29
Spect.3	24.79	25	18.28	22.58	0.28	0.1

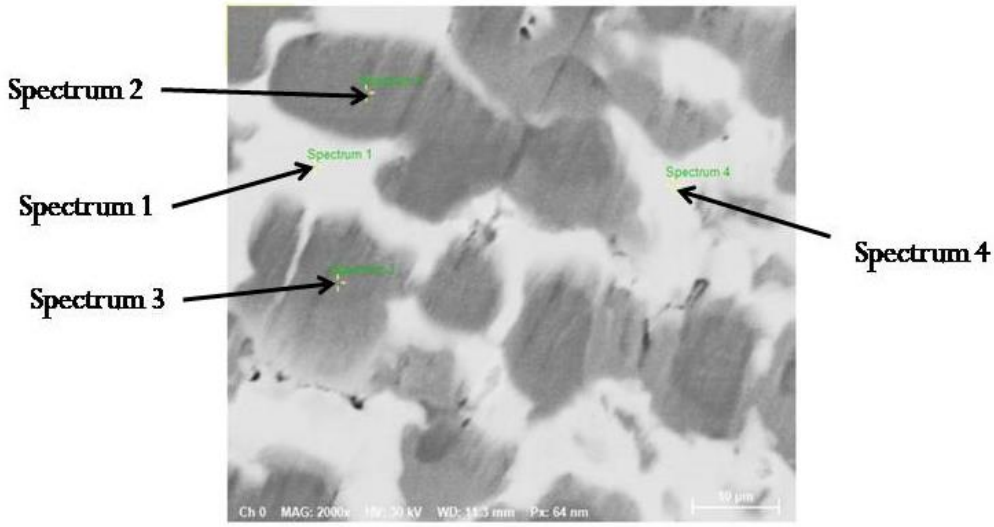

Fig. 6.14 EDS mapping of $FeCoNiCrCuZr_{7.5}$

Table 6.8

Element	Fe	Co	Ni	Cr	Cu	Zr
Spect.1	14.29	17	25.96	4.45	19.37	18.92
Spect.2	37.45	12.59	5.41	41.28	2.57	0.7
Spect.3	37.00	13.24	5.52	40.99	2.69	0.56
Spect.4	14.56	17.50	25.98	5.36	19.55	17.05

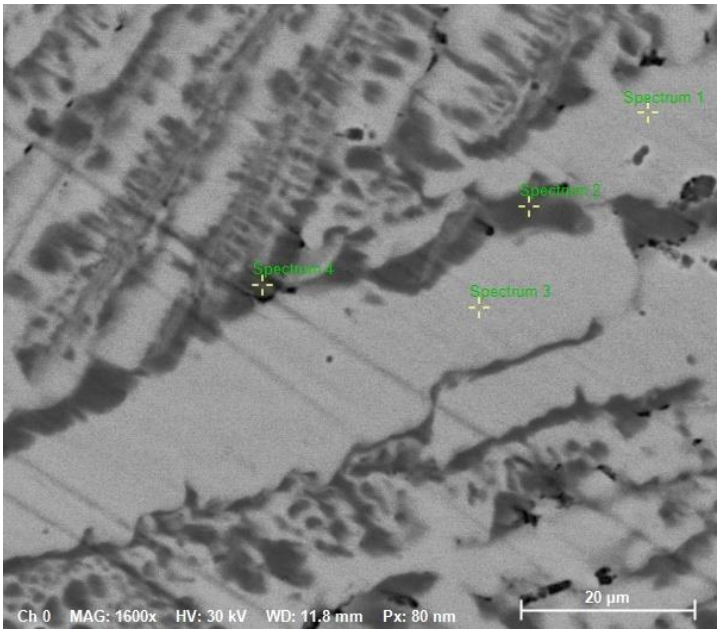

Fig. 6.15 EDS mapping of $FeCoNiCrCuZr_{10}$

Table 6.9

Element	Fe	Co	Ni	Cr	Cu	Zr
Spect.1	10.35	23.84	30.18	1.97	15.83	17.83
Spect.2	28.56	22.46	13.74	12.56	20.97	1.72
Spect.3	10.14	24.12	29.74	1.78	15.09	19.13
Spect.4	31.68	25.26	14.64	13.98	12.81	1.63

6.3 Characterization of multicomponent alloys, synthesized through chemical route

6.3.1 Structural characterization of binary alloys

X-ray diffraction (XRD) analysis was used to identify the phase and crystallinity of nanoparticles. The XRD patterns of CuNi nanoparticles prepared by chemical routes are shown in figure 6.16a. The sharp diffraction peak emerges at 2θ angles of 43.469°, 51.8° ,72.4° and 90° for polyol synthesized CuNi nanoparticles, corresponds to 111, 200 , 220 and 113 crystal planes, respectively, suggesting face-centered cubical structure

(ICSD: 628549). Some minor peaks at 31.5°, 34.3° and 45.1° corresponding to impurities present in the samples.

6.3.2 Spectroscopic analysis of binary alloys

FTIR spectroscopy is used to study the interaction between different species and changes in chemical environment of the mixture. Figure 6.16b shows the FTIR spectra of CuNi nanoparticles synthesized by chemical and chemical routes recorded in the range of 400-4000 cm^{-1}. The FTIR spectrum of CuNi nanoparticles synthesized by chemical route exhibits an absorption band at 1575, 1220, 1065, 772 and 384 cm^{-1} which refers to CuO stretching, NiO stretching, stretching vibration of -CHO group and CuNi stretching, respectively.[32]

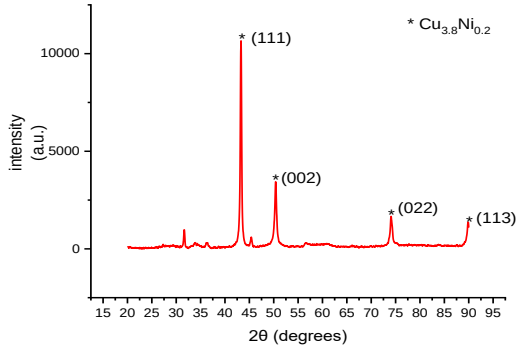

a

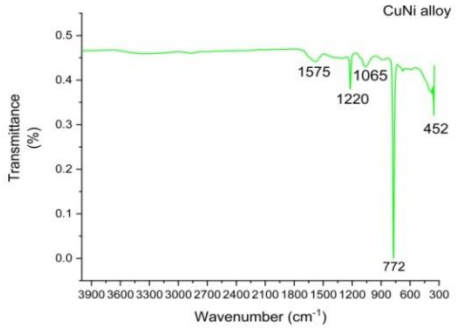

b

Fig. 6.16 a) X-ray diffraction pattern b) FTIR pattern for CuNi alloy

6.3.3 Structural and spectroscopic characterization of ternary alloys

The X-ray diffraction (XRD) patterns of FeCuNi nanoparticles prepared by chemical routes are shown in figure 6.17a. The sharp diffraction peak emerges at 2θ angles of 42.81°, 50.8° and 72.4° for polyol synthesized FeCuNi nanoparticles, corresponds to 111, 200 and 220crystal planes, respectively, showing face-centered cubical structure for copper (ICSD: 53755). The peaks emerge at 2θ values of 44.836°, 65.536° and 83.26° corresponds to 011 ,002 and 112 crystal planes, respectively, revealing body centered cubic structure for iron (ICSD: 631728). Similar peaks emerge at 2θ values of 43.695°, 56.082° and 74.827° corresponds to 111, 002 and 022 crystal planes suggesting face centered cubic structure for gamma nickel (ICSD: 1633554). Peaks emerging at 26.744°, 31.144° and 35.382° show cubic structure for $FeCO_3$.

From the figure 6.17b shows the FTIR spectra of FeCuNi nanoparticles synthesized by chemical routes recorded in the range of 400-4000 cm^{-1}. The IR spectrum of FeCuNi nanoparticles synthesized by chemical means covers a transmittance band at 1597, 1066,762 and 589 cm^{-1} which refers to NiO stretching, stretching vibration of -CHO group, CuNi stretching, and FeO stretching, respectively. Fig 6.17 c and d shows SEM image and EDS mapping of FeCuNi alloy.

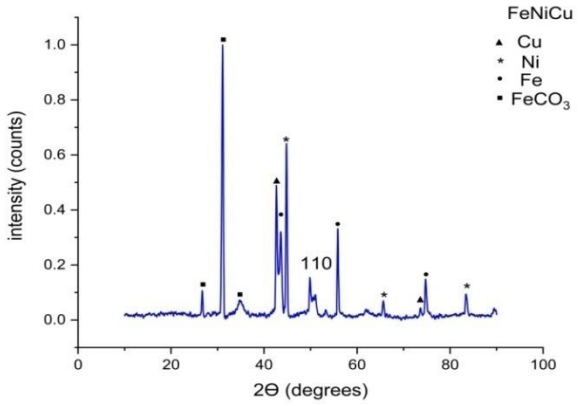

a

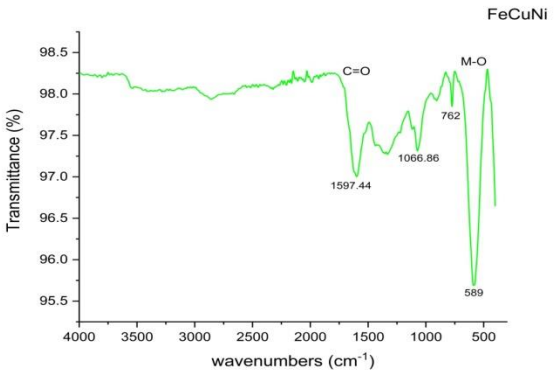

b

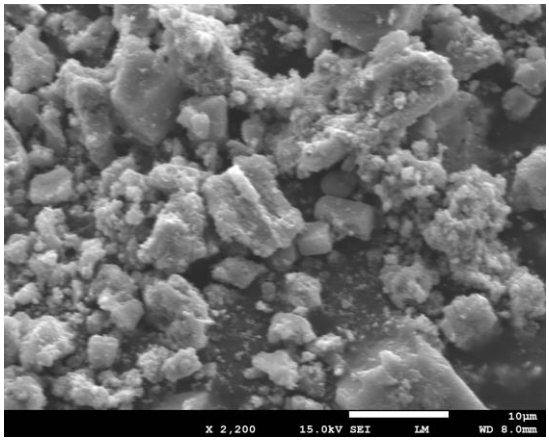

c

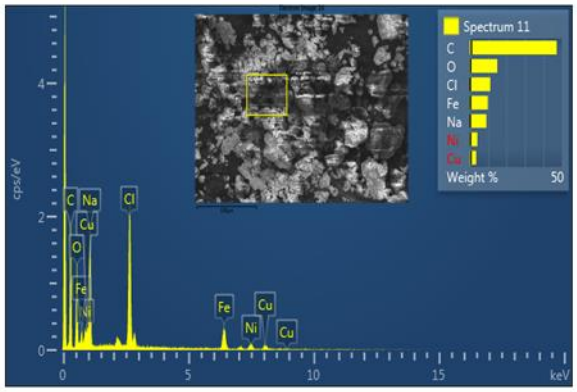

Elements	Weight %
Fe	9.82
Ni	4.17
Cu	3.49
C	47.25
O	14.97

d

Fig. 6.17 a) X– ray diffraction for FeNiCu b) FTIR spectrum of FeNiCu alloy

c) SEM image of FeNiCu d) EDS image of FeCuNi alloy

The X-ray diffraction (XRD) patterns of CoNiCr nanoparticles prepared by chemical routes are shown in figure 6.18a. The sharp diffraction peak emerges at 2θ angles of 44.21°, 64.30° and 81.35° for polyol synthesized CoNiCr nanoparticles, corresponds to 011, 002 and 112 crystal planes, respectively, suggesting cubical structure for chromium (ICSD: 53798). Similarly, peaks emerges at 2θ values of 41.80°, 48.65°, 71.26° and 86.17° corresponds to 111,002,022 and 113 crystal planes, respectively, suggesting cubic structure for nickel hydride (ICSD: 56077). Similarly, peaks emerge at 2θ values of 37.282°, 43.33°, 62.917°and 75.57° corresponds to 101, 012,110 and 113 crystal planes suggesting hexagonal structure for nickel oxide (ICSD: 92130). Cobalt has hexagonal structure having peaks at 2θ values of 25.04°, 32.61°, 38.59° , 42.787° , 66.07° , 76.31° and 76.66° corresponding to 012, 104, 110, 113, 214, 00 12 and 217 (ICSD: 61066). Metastable cobalt of hexagonal structure is also observed at peaks of 2θ values of 33.99°, 40.53°, 41.41° and 43.649° corresponding to 004, 114, 032 and 220 crystal planes, respectively (ICSD: 52933).

Figure 6.18b shows the IR spectra of CoNiCr nanoparticles synthesized by chemical routes recorded in the range of 400-4000 cm^{-1}. The IR spectrum of CoNiCr nanoparticles synthesized by chemical means covers antransmittance band at 3339, 2874, 1602, 1462, 1356, 1124, 1060, 900 and 616 cm^{-1} which refers to -OH stretching, -CH stretching vibration, C=C stretching, -CHO stretching, -NiH stretching and last two may be for some metal oxides stretching, respectively. Fig 6.17 c and d shows SEM image and EDS mapping of CoNiCr alloy.

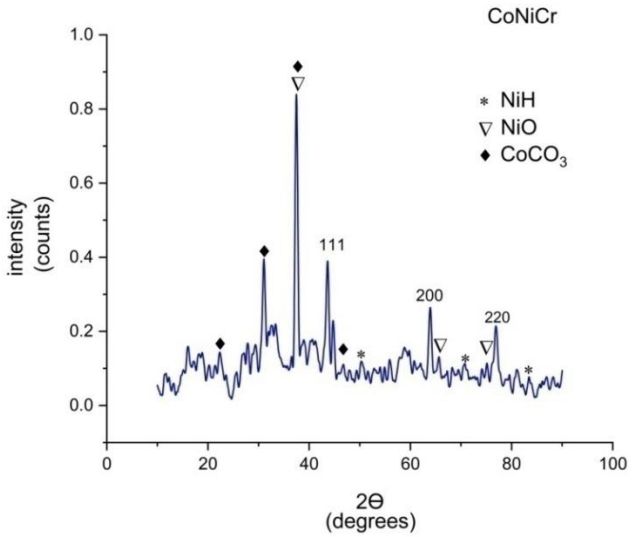
CoNiCr
* NiH
▽ NiO
♦ $CoCO_3$
intensity (counts)
111
200
220
2Θ (degrees)

a

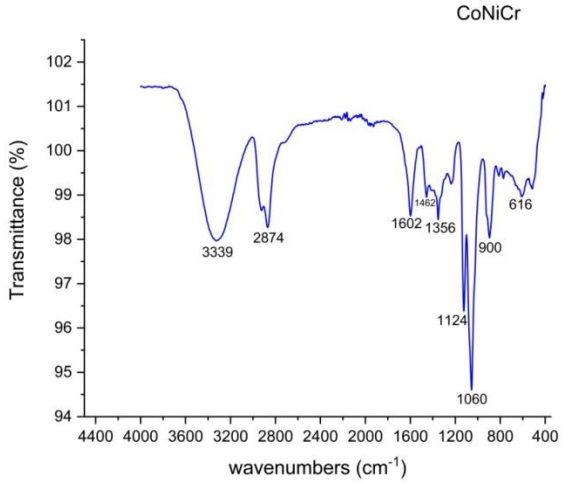
CoNiCr
Transmittance (%)
3339
2874
1602
1482
1356
1124
1060
900
616
wavenumbers (cm^{-1})

b

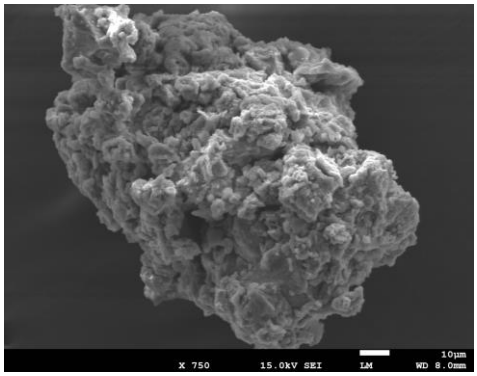
X 750
15.0kV SEI
LM
10µm
WD 8.0mm

c

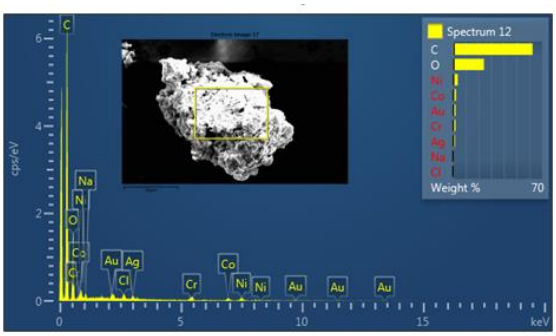

Elements	Weight %
Co	2.33
Ni	3.77
Cr	1.98
C	62.59
O	24.33

d

Fig. 6.18 a) X– ray diffraction for CoNiCr b) FTIR spectrum of CoNiCr alloy

c) SEM image of CoNiCr alloy d) EDS mapping of CoNiCr alloy

The X- ray diffraction pattern of CoNiCu nanoparticles synthesized through polyol process is represented by fig. 6.19a. The sharp diffraction peak emerges at 2θ angles of 43.2°, 50.30°, 73.88° and 89.62° for polyol synthesized CoNiCu nanoparticles, corresponds to 111, 002, 022 and 113 crystal planes, respectively, suggesting face centered cubical structure for copper (ICSD: 53246). Similarly, sharp peaks at 2θ values of 45.502°, 53.045° and 78.324°, corresponds to the crystal plane 111, 002 and 022, respectively, revealing face centered cubic structure for nickel (ICSD: 41508). Similarly, same peaks at 2θ values of 16.50°, 24.86°, 31.57°, 38.95° and 39.707°, corresponds to the crystal plane 002, 003, 200 ,111 and 112, respectively, revealing monoclinic structure for cobalt dioxide (ICSD: 95440). Similarly peaks at 2θ values of 13.35°, 18.2°, 28.37°, 30.19°, 34.303° , 44.039° and 55.1° , corresponds to 010, 111, 212, 113, 311, 304 and 132 respectively, revealing orthorhombic structure for $CuC_2H_6O_7$ (ICSD : 240734).

Figure 6.19b shows the IR spectra of CoNiCu nanoparticles synthesized by chemical routes recorded in the range of 400-4000 cm^{-1}. The IR spectrum of CoNiCu nanoparticles synthesized by chemical means covers an transmittance band at 3320, 2868, 1590, 1354, 1056, 904, 618 and 518 cm^{-1} which refers to -OH stretching vibration, stretching vibration of -CH group, C=C stretching vibration, stretching vibration -CHO group,

stretching vibration of ether (C-O-C) group and last three belong to some metallic oxide stretching, respectively. Fig 6.17 c and d shows SEM image and EDS mapping of CoCuNi alloy.

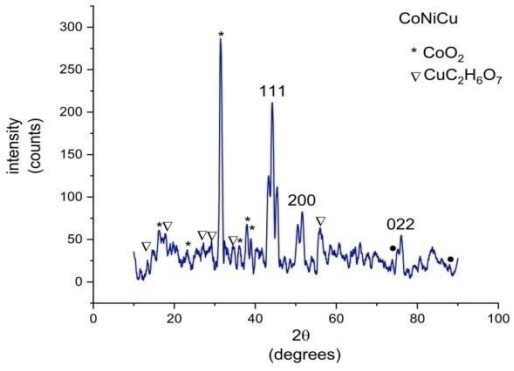

a

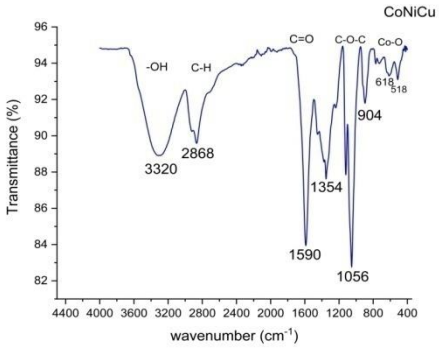

b

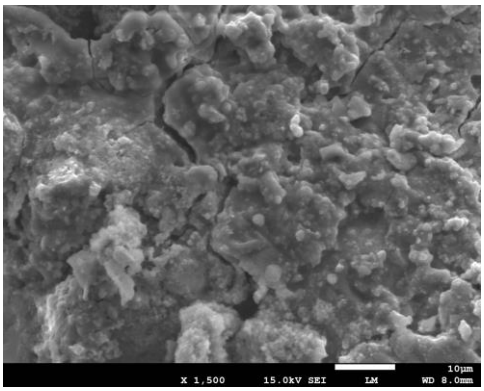

c

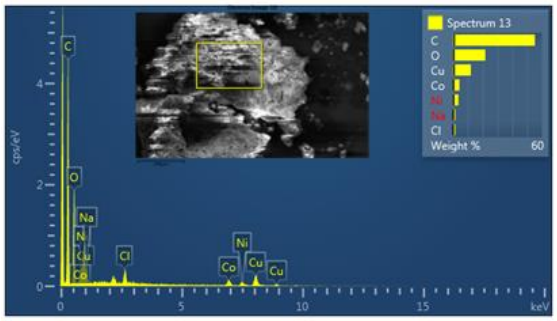

Elements	Weight %
Co	4.43
Ni	3.72
Cu	12.09
C	55.19
N	21.73

d

Fig. 6.19 a) XRD pattern of CoNiCu b) FTIR spectrum of CoNiCu

c) SEM images of CoNiCu d) EDS mapping of CoNiCu alloy

6.3.4 Structural and spectroscopic characterization of quaternary alloys

The X-ray diffraction (XRD) pattern for FeCoNiCu alloy synthesized through chemical route is shown in fig. 6.20a. The 2θ values of 43.30°, 50.42°, 74.1° and 89.87°, corresponds to 111, 002 , 022 and 113 crystal planes respectively, revealing face centered cubic structure of copper (ICSD: 53757). Similarly the XRD peaks at 2θ values of 45.46°, 66.25° and 84.03°, corresponds to 011, 002 and 112 crystal planes, respectively, revealing body centered cubic structure of iron(ICSD: 159354). There is formation of $Cu_{3.8}Ni_{0.2}$, revealed by the XRD peaks of 2θ values of 43.47°, 50.63° and 74.42° corresponds to 111, 002 and 022 crystal planes having face centered cubic structure(ICSD: 628549). The XRD peaks at 24.87°, 29.46°, 30.54°, 31.96° and 32.57° is related to 130, 223, 040 and 125 crystal planes, respectively, showing formation of orthorhombic structure cobalt carbonyl ($Co_4(CO)_{12}$) (ICSD: 88529). Similarly the formation of orthorhombic structure iron carbide ($Fe_4C_{0.63}$) was revealed through the XRD peaks at 2θ values of 43.51°, 45.20°, 60.54°, 65.85° and 78.68° , corresponding to 11 12 , 020 , 021 , 00 24 and 220 crystal planes respectively(ICSD: 9860). The XRD pattern of FeCoNiCu suggests the reduction of some cuprous chloride and ferric chloride into copper and

iron while formation of cobalt carbonyl shows that polyols at 180 ̊C is not reduced cobalt chloride into cobalt.

The FTIR spectrum of FeCoNiCu is represented by fig. 6.20b. The IR spectra of FeCoNiCu alloy prepared through chemical route was recorded in the range of 4000-400cm^{-1}. The IR spectrum of FeCoNiCu covers transmittance band at 3354, 2920, 1623, 1372, 1054, 890 and 662 cm^{-1} which corresponds to –OH group stretching, -CH stretching vibration, C=O stretching vibration, C-Cl (halogenated group), C-O-C (ether group) and last two belong to organometallic group.

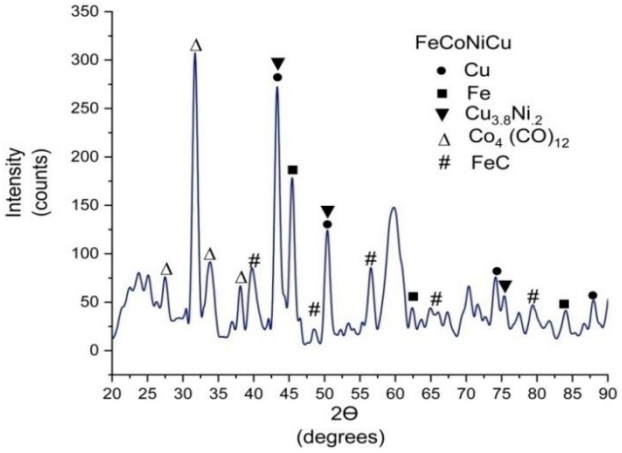

a

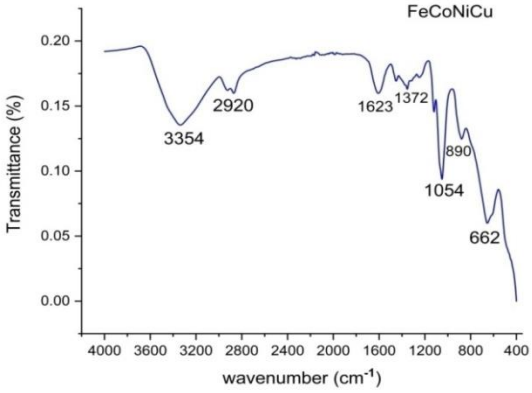

b

Fig. 6.20 a) XRD pattern b) FTIR spectra of FeCoNiCu alloy

Chapter 7

Mechanical Properties of HEAs

7.1 Hardness measurements of the HEAs

The hardness of the developed HEAs have been measured using Vickers Hardness tester was performed on the samples to determine the mechanical properties. At least five measurements were carried out for each sample. The average value with error bars indicating the standard deviation has been indicated in the figure. Fig. 7.1, 7.2, 7.3 show the plot of hardness value w.r.t. Zr concentration for the developed $FeCoNiCrZr_x$, $FeCoNiCrAlZr_x$ and $FeCoNiCrCuZr_x$ HEAs system. From the Bar chart (Figure 7), it can be clearly seen that hardness value of the HEAs increases with the increase of Zr content. The hardness value of FeCoNiCr alloy system as shown in bar chart (Figure 7.1) is lowest as compared to other HEAs without addition of Zr. This is attributed to the presence of single face centered cubic (FCC) solid solution phase. While it is observed that the hardness value for FeCoNiCrAl ((Figure 7.2) is higher as compared to other HEAs without addition of Zr. This is because of the presence of body centered cubic (BCC) solid solution phase. It is also observed that with addition of Zr, hardness value increases (as shown in Figure 7.1, 7.2, 7.3). It is to be noted that the eutectic microstructure develops with addition of Zr. The eutectic microstructure consists of solid solution phase (FCC or BCC) and intermetallic compound. Therefore, the high value of hardness is attributed to several factors such as solid solution phase, intermetallic compound, eutectic morphology, fineness of microstructure.

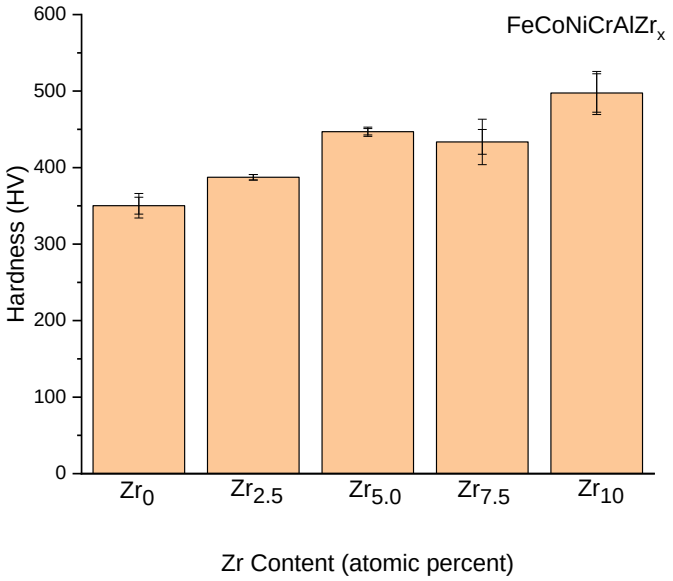

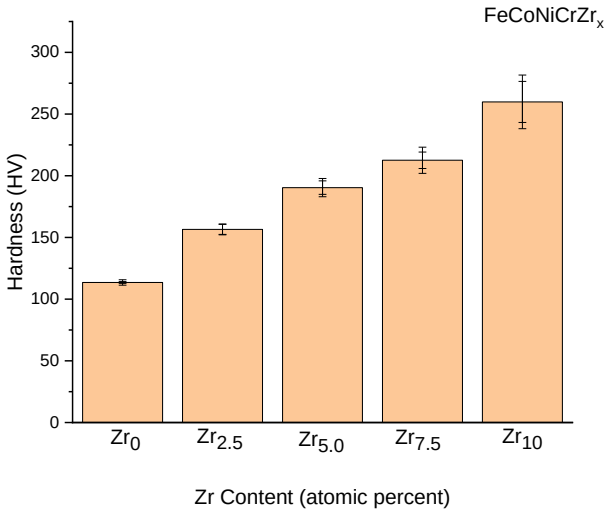

Bar chart 7.1 shows Hardness value for $FeCoNiCrZr_x$ (X = 0, 2.5, 5.0, 7.5, 10) HEAs

Bar chart 7.2 shows Hardness value for $FeCoNiCrAlZr_x$(X = 0, 2.5, 5.0, 7.5, 10) HEAs

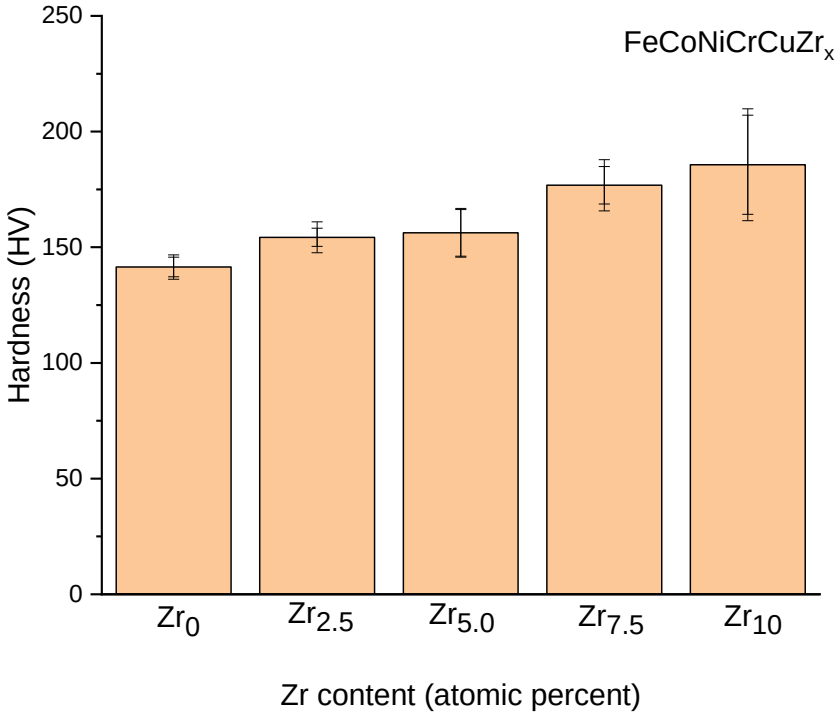

Bar chart 7.3 shows Hardness value for FeCoNiCrCuZr$_x$(X = 0, 2.5, 5.0, 7.5, 10) HEAs

7.2 Hot Deformation Behavior

The true stress-strain curves of the multicomponent of BCC FeCoNiCrAl HEA at different temperatures (700^{o}C, 800^{o}C, 900^{o}C, 1000^{o}C, 1050^{o}C, 1100^{o}C and at fixed strain rate of 10^{-1} s^{-1} were obtained for the suction cast cylinder samples with diameter (ϕ) = 6 mm having an aspect ratio of 1.5:1. Figure 7.4 shows the true stress strain curve of BCC FeCoNiCrAl HEA at various temperatures with constant strain rate. It is also evident from figure 7.4 that the flow stress decreases with increase in temperature at a given strain rate ($\dot{\varepsilon}$).The flow stress reaches a maximum value at a critical strain followed by a softening that continues up to a strain of 0.7. The drop in stress value after yield point could be due to dynamic recrystallization, which in general is attributed to softening during hot deformation.

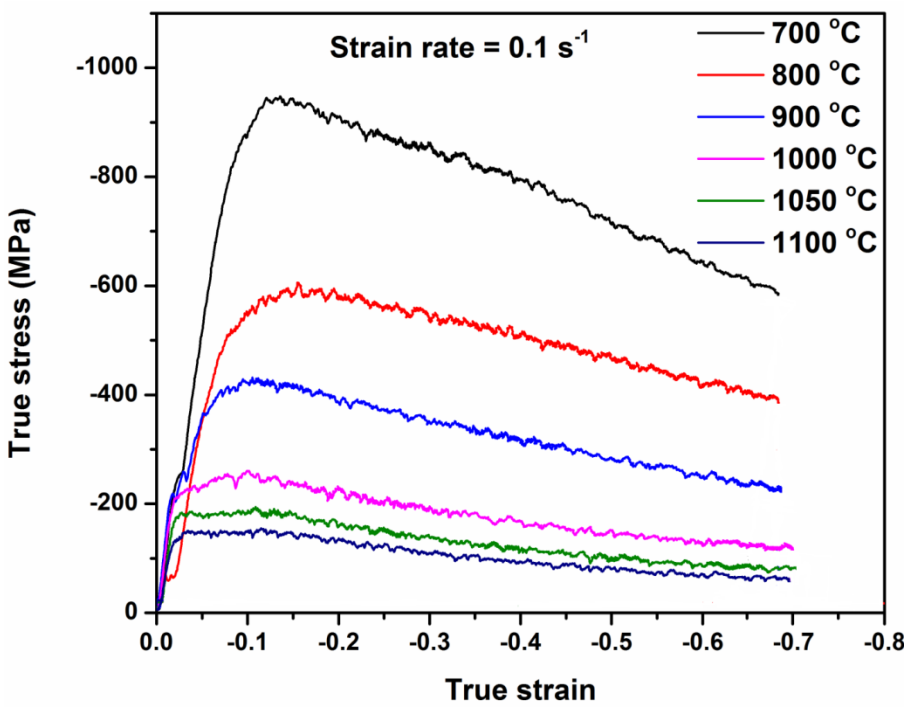

Fig. 7.4 True stress – true strain plots of BCC FeCoNiCrAl HEA at different temperatures and constant strain rate of $0.1s^{-1}$.

Chapter 8

Conclusions and Future Scope

8.1 Conclusion

Based upon results and discussion on the developed HEAs, the following conclusion can be drawn:

I. The high entropy alloys have been successfully prepared by solidification technique.

II. Solidification pathways for $FeCoNiCrZr_{10}$ and $FeCoNiCrCuZr_{10}$ have been determined using Thermocal simulations.

III. Effect of Zr on the morphology of the HEA is studied by using thermodynamic and Hume Rothery parameters.

IV. Microstructural analysis of Zr containing alloys is done. $FeCoNiCrZr_x$ shows a unique bimodal eutectic structure while $FeCoNiCrCuZr_x$ gives a hypereutectic structure with a acicular structure.

V. Hardness test result shows that hardness value increases with increase of Zr content. This happen due to formation of eutectic structure, intermetallics and solid solution.

VI. Highest hardness value is 497.5 HV of $FeCoNiCrAlZr_{10}$. This is due to formation of BCC solid solution and intermetallics along with eutectic structure.

VII. The lowest hardness value is 113.52HV of FeCoNiCr because it consists of single FCC solid solution phase only.

VIII. By Polyol process, binary alloy($Cu_{3.8}Ni_{0.2}$) was synthesized successfully along with some ternary alloys like FeNiCu and CoNiCu. XRD pattern clearly shows formation of some type of solid solution for the alloys.

IX. Some ternary alloys such as CoNiCr and quaternary alloys like FeCoNiCu doesn't form solid solution as required due to large difference in the reduction potential of the elements.

8.2 Scope for future work

I. Mechanical behavior study, especially hot deformation behavior, of $FeCoNiCrZr_{10}$, $FeCoNiCrAlZr_{10}$ and $FeCoNiCrCuZr_{10}$ will be taken into consideration.

II. More experiments on the Polyol process special in-situ experiments must be done for the synthesis of HEA nanoparticles. This will give us the clear ideal about way in which our reaction is proceeding.

References

[1] Yeh J. W. et al. (2004),Nanostructured high-entropy alloys with multiple principal elements: Novel alloy design concepts and outcomes, Adv. Eng. Mater.6, 299-303.

[2] Cantor B. (2014),Multicomponent and high entropy alloys, Entropy 16,4749–4768.

[3] Cantor B., Chang I. T. H., Knight P., Vincent A. J. B. (2004) Microstructural development in equiatomic multicomponent alloys, Mater. Sci. Eng. A 375–377, 213–218.

[4] Murty B.S., Yeh J.W., Ranganathan S.(2014),High Entropy Alloy, Butterworth-Heinemann,pp. 3-55.

[5] Jain R., Rahul M. R., Jain S., Samal S., Kumar V.(2018),Phase Evolution and Mechanical Behaviour of Co–Fe–Mn–Ni–Ti Eutectic High Entropy Alloys, Trans. Indian Inst. Met., 71, 2795–2799.

[6] Zhang Y. et al. (2014),Microstructures and properties of high-entropy alloys, Prog. Mater. Sci. 61, 1–93.

[7] Guo S., Ng C., Lu J., Liu C. T. (2010),Effect of valence electron concentration on stability of fcc or bcc phase in high entropy alloys, J. Appl. Phys 109, 10.

[8] Hemphill M. A. et al.(2012),Fatigue behavior of Al 0.5CoCrCuFeNi high entropy alloys, Acta Mater. 60,5723–5734.

[9] Zhang Y., Zuo T., Cheng Y., Liaw P. K., High-entropy alloys with high saturation magnetization, electrical resistivity, and malleability, Sci. Rep. 3,1–7.

[10] Gludovatz B., Hohenwarter A.,Catoor D., Chang E. H., George E. P., Ritchie R. O. (2014), A fracture-resistant high-entropy alloy for

cryogenic applications, Science 345, 1153–1158.

[11] Lim X.(2016),Metal mixology - Stronger, tougher, stretchier: with a simple new recipe, metallurgists are creating a generation of alloys with remarkable properties, Nature 533, 306–307.

[12] Li Z.et al (2016),Metastable high-entropy dual-phase alloys overcome the strength-ductility trade-off., Nature 534,227–230.

[13] Hsu C. Y. et al (2011),On the superior hot hardness and softening resistance of AlCoCr xFeMo 0.5Ni high-entropy alloys, Mater. Sci. Eng. A 528, 3581–3588.

[14] Tsai K. Y.,Tsai M. H., Yeh J. W. (2013), Sluggish diffusion in Co-Cr-Fe-Mn-Ni high-entropy alloys, Acta Mater., 61, 4887–4897.

[15] Wang F., Zhang Y., Chen G., Davies H.A. (2009),Tensile and compressive mechanical behavior of a cocrcufenial 0.5 high entropy alloy ,. J. Mod. Phys. B 23, 1254–1259.

[16] Otto F. et al (2013),The influences of temperature and microstructure on the tensile properties of a CoCrFeMnNi high-entropy alloy, Acta Mater. 61,5743–5755.

[17] Senkov O. N. et al (2010),Refractory high-entropy alloys, Intermetallics 18, 1758–1765.

[18] Kuznetsov A. V. et al (2012),Tensile properties of an AlCrCuNiFeCo high-entropy alloy in as-cast and wrought conditions, Mater. Sci. Eng. A 533, 107–118.

[19] Tong C.J. et al (2007),Mechanical performance of the Al x CoCrCuFeNi high-entropy alloy system with multiprincipal elements, Metall. Mater. Trans. A 36,1263–1271.

[20] Lu Y.et al (2014),A promising new class of high-temperature

alloys: Eutectic high-entropy alloys, Sci. Rep. 4, 1–5.

[21] P. Solidification, Principals of solidification. .

[22] Guo T. ,Tan Y. (2013),Formation of one-dimensional Ag-Au solid solution colloids with Au nanorods as seeds, their alloying mechanisms, and surface plasmon resonances, Nanoscale 5, 561–569.

[23] Zhang K. B. et al.(2009),Nanocrystalline CoCrFeNiCuAl high-entropy solid solution synthesized by mechanical alloying, J. Alloys Compd. 485, 34–37.

[24] Zhang K. B. et al (2010),Characterization of nanocrystalline CoCrFeNiTiAl high-entropy solid solution processed by mechanical alloying, J. Alloys Compd. 495, 33–38.

[25] Eid K., Wang H., Wang L.(2016), Nanoarchitectonic Metals. Elsevier Inc.16, 55-56.

[26] Chatterjee J. et al (2005),Synthesis and characterization of polymer encapsulated Cu-Ni magnetic nanoparticles for hyperthermia applications, J. Magn. Magn. Mater. 293, 303–309.

[27] Gali A. , George E. P. (2013),Tensile properties of high- and medium-entropy alloys, Intermetallics 39, 74–78.

[28] Zhang Y. , Zhou Y. J. (2007),Solid Solution Formation Criteria for High Entropy Alloys, Mater. Sci. Forum 561–565, 1337–1339.

[29] Yang X. ,Zhang Y. (2012),Prediction of high-entropy stabilized solid-solution in multi-component alloys, Mater. Chem. Phy. 132, 233–238.

[30] Singh A. K. et al (2014),A geometrical parameter for the formation of disordered solid solutions in multi-component alloys,

Intermetallics 53, 112–119.

[31] Saal J. E. et al (2018), Equilibrium high entropy alloy phase stability from experiments and thermodynamic modeling, Scr. Mater. 146, 5–8.

[32] Ahmed J. et at (2008),Bimetallic Cu-Ni nanoparticles of varying composition (CuNi3, CuNi, Cu3Ni), Colloids Surfaces A Physicochem. Eng. Asp. 331, 206–212.